



저작자표시-비영리-변경금지 2.0 대한민국

이용자는 아래의 조건을 따르는 경우에 한하여 자유롭게

- 이 저작물을 복제, 배포, 전송, 전시, 공연 및 방송할 수 있습니다.

다음과 같은 조건을 따라야 합니다:



저작자표시. 귀하는 원저작자를 표시하여야 합니다.



비영리. 귀하는 이 저작물을 영리 목적으로 이용할 수 없습니다.



변경금지. 귀하는 이 저작물을 개작, 변형 또는 가공할 수 없습니다.

- 귀하는, 이 저작물의 재이용이나 배포의 경우, 이 저작물에 적용된 이용허락조건을 명확하게 나타내어야 합니다.
- 저작권자로부터 별도의 허가를 받으면 이러한 조건들은 적용되지 않습니다.

저작권법에 따른 이용자의 권리는 위의 내용에 의하여 영향을 받지 않습니다.

이것은 [이용허락규약\(Legal Code\)](#)을 이해하기 쉽게 요약한 것입니다.

[Disclaimer](#)

Influence of Al and Mn additions on the
microstructure and corrosion properties of extruded
Mg–8Sn–1Zn alloys

Hyeon Ju Kim

Department of Materials Science Engineering

Graduate school of UNIST

Influence of Al and Mn additions on the
microstructure and corrosion properties of extruded
Mg–8Sn–1Zn alloys

A thesis

submitted to the Graduate School of UNIST

in partial fulfillment of the

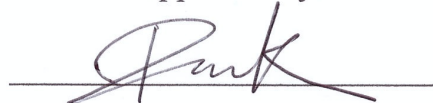
requirements for the degree of

Master of Science

Hyeon Ju Kim

12. 11. 2014

Approved by



Advisor

Sung Soo Park

Influence of Al and Mn additions on the
microstructure and corrosion properties of extruded
Mg-8Sn-1Zn alloys

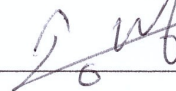
Hyeon Ju Kim

This certifies that the thesis of Hyeon Ju Kim is approved.

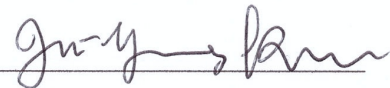
12. 11. 2014



Advisor : Sung Soo Park



Myoung Hoon Song



Ju-Young Kim

Abstract

The microstructure and corrosion properties of extruded Mg–8Sn–1Zn alloys with varying Al contents were investigated. The microstructures of the extruded alloys mainly consisted of α -Mg grains and Mg₂Sn particles in common. The addition of Al to the ternary alloy resulted in the formation of different types of Al–Fe-based intermetallic particles depending on Al contents. Corrosion rates were found to be drastically increased by additions of 1 – 3wt% Al. The extruded alloys with 1 – 3wt% Al showed over 30 times higher corrosion rates than those containing less than 0.3wt% Al in 0.6 M NaCl solution. The increase in corrosion rate produced by the Al addition was attributed to the presence of Al₃Fe₂ particles, which act as strong cathodic sites for H₂ evolution during corrosion.

In addition, a solution to reduce the high corrosion rate of the Mg–8Sn–1Zn alloys containing Al is suggested. The presence of Al₃Fe₂ particles, having deleterious effect on corrosion resistance, can be replaced by that of Al₈Mn₅ particles by the addition of Mn to the Mg–8Sn–1Zn alloys with 1 – 3wt% Al. The Mg–8Sn–1Zn–1Al alloy with 0.1wt%Mn showed over an order lower corrosion rate than the quaternary alloy without Mn, which can be attributed to the relatively sluggish cathodic reaction in the presence of Al₈Mn₅ particles.

Contents

I. Introduction	
1.1. Mg-Sn based alloys	1
1.2. Mn alloying element	3
II. Theoretical review	
2.1. Corrosion of magnesium	4
2.2. Corrosion mechanism of magnesium	6
2.3. Material factors affecting corrosion of magnesium	12
2.4. Evaluation of corrosion behavior	17
III. Influence of Al addition	
3.1. Introduction	21
3.2. Experimental	22
3.3. Results	24
3.4. Discussion	37
IV. Influence of Mn addition	
4.1. Introduction	40
4.2. Experimental	40
4.3. Results	43
4.4. Discussion	52
V. Conclusions	
VI. References	

List of figures

Fig. 1. Potential-pH (Pourbaix) diagram for magnesium in 25 degree Celsius water.

Fig. 2. Schematic diagram of micro-galvanic corrosion.

Fig. 3. Schematic diagram of pitting corrosion for AM60 alloy.

Fig. 4. Image of filiform corrosion.

Fig. 5. Schematic diagram of intergranular corrosion.

Fig. 6. Image of intergranular corrosion.

Fig. 7. Influence E_{corr} by adding various elements on AZ91 alloy.

Fig. 8. Influence I_{corr} by adding various elements on AZ91 alloy.

Fig. 9. Schematic diagram of immersion test.

Fig. 10. Schematic diagram of 3-electrode cell which uses for potentiodynamic test.

Fig. 11. Polarization curve.

Fig. 12. Schematic diagram of hydrogen evolution test.

Fig. 13. Optical micrographs of the extruded alloys: (a) TZ81, (b) TZA810, (c) TZA811, and (d) TZA813.

Fig. 14. XRD patterns showing the presence of Mg and Mg_2Sn phases in the extruded alloys.

Fig. 15. SEM micrographs of the extruded alloy: (a) TZ81, (b) TZA810, (c) TZA811, and (d) TZA813. Particles labeled A-C were observed in the TZA810, TZA811, and TZA 813 alloys, respectively.

Fig. 16. (a) TEM micrographs showing the particles A-C in Fig. 15. (b) EDS spectra and (c) electron diffraction patterns from the particles.

Fig. 17. Optical micrographs showing the macroscopic surfaces of the extruded alloys before and after immersion in 0.6M NaCl solution: (a) TZ81, (b) TZA810, (c) TZA811, and (d) TZA813.

Fig. 18. SEM micrographs showing the surfaces of the extruded alloys before and after immersion in 0.6 M NaCl solution: the TZA810 alloy (a) before and (b) after immersion for 20 minutes, the TZA811 alloy (c) before and (d) after immersion for 4 minutes, and the TZA813 alloy (e) before and (f) after immersion for 4 minutes.

Fig. 19. Corrosion rates of the extruded alloys with different Al contents, which were measured by immersion in 0.6 M NaCl solution for 72 hours.

Fig. 20. Corrosion potential transition curves of the extruded alloys.

Fig. 21. (a) Polarization curves of the extruded alloys in 0.6 M NaCl solution and (b) cathodic current density values measured from the polarization curves at -1.80 V SCE .

Fig. 22. (a) Corrosion potential transition curves and (b) polarization curves of the extruded alloys in 0.005 M NaCl solution with (c) pitting potential values and (d) cathodic current density values from the polarization curves.

Fig. 23. SKPFM images of the (a) TZA810 and (b) TZA811 alloys and corresponding Volta potential profiles along lines A–D in (a) and (b).

Fig. 24. (a) Optical micrograph, (b) SEM micrograph of the extruded TZAM8110 alloy and (c) EDS spectra of particle labeled A in the TZAM8110 alloy

Fig. 25. EPMA images of the (a) TZA811 and (b) TZAM8110 alloys and corresponding Al, Fe, Mn mapping images.

Fig. 26. (a) TEM micrographs of Particle A, corresponding (b) Al, (c) Fe, (d) Mn mapping images, and electron diffraction patterns of (e) '1' region, (f) '2' region.

Fig. 27. Optical micrographs showing the macroscopic surfaces of the TZAM8110 extruded alloy before and after immersion in 0.6 M NaCl solution.

Fig. 28. SEM micrographs showing the surfaces of the extruded alloys before and after immersion in 0.6 M NaCl solution: the TZA811 alloy (a) before and (b) after immersion for 4 minutes, and the TZAM8110 alloy (c) before and (d) after immersion for 20 minutes.

Fig. 29. Corrosion rates of the extruded TZA811 and TZAM8110 alloys which were measured by hydrogen evolution test and immersion test in 0.6 M NaCl solution.

Fig. 30. Polarization curves of the extruded TZA811 and TZAM8110 alloys in 0.6 M NaCl solution.

Fig. 31. SKPFM images of the TZAM8110 alloy and corresponding Volta potential profiles along lines A–B.

List of tables

Table 1. Corrosion potential of engineering metals.

Table 2. Corrosion potential of magnesium and its second particles in 5% NaCl solution (pH 10.5).

Table 3. Corrosion rates at E_{corr} in 1N NaCl solution.

Table 4. Influence of alloying elements on magnesium alloys.

Table 5. Influence of alloying elements on magnesium alloys (2).

Table 6. The constants (K) in corrosion rate equation.

Table 7. Nominal and analyzed compositions (wt%) of the extruded alloys investigated in this study.

I. Introduction

Magnesium and magnesium alloys have attracted considerable attention in industrial application due to their outstanding mechanical properties. Magnesium and magnesium alloys have high specific strength, high thermal conductivity, high damping characteristics, good machinability and favorable biocompatibility. Among those properties, the high strength to weight ratio and low density cause an increase in the demand for magnesium in automotive, and aerospace application [1]. The density of magnesium is much lower than aluminum and iron which are commercialized in industry. The reduction of the weight through magnesium alloy commercialization will produce the positive effects, such as fuel efficiency and energy conservation.

However, magnesium and magnesium alloys have some barriers to commercialize. One of the limitations is the corrosion properties [2]. Therefore the research into improving the corrosion properties of magnesium and its alloys is necessary.

1.1. Mg-Sn based alloys

Among the various Mg alloys, Mg-Sn-based alloys have recently attracted great interest due to their excellent creep resistance at elevated temperatures [3–7]. So many researchers has been researching Mg-Sn based alloys. The outstanding properties of Mg-Sn based alloy are also reported. Kang et al. triggered this development of Mg-Sn-based alloys with improved creep resistance by presenting new Mg-Sn-Al-Si alloys which contained Mg_2Sn particles along grain boundaries as well as within the Mg matrix in the cast condition [3,4]. Their anti-creep properties mainly result from the presence of the thermally stable Mg_2Sn particles along grain boundaries, which prevent creep deformation via grain boundary sliding.

Interest in development of Mg-Sn-based alloys is continuing further because of the strong demands for weight reduction in the automotive and aerospace industries. More recently, it has been shown that the Mg-Sn-based alloys have great mechanical properties such as high strength and good plasticity [8-16], confirming the potential for the development of wrought Mg products as well.

In extruded Mg-Sn-based alloys, Sn content is one of the important factors influencing mechanical properties [8,9]. W.L. Cheng et al. found that tensile and compressive strengths increase and yield asymmetry between tension and compression reduces as the Sn content increases. This is due to grain

refinement and an increase in the volume fraction of Mg₂Sn particles with the addition of Sn [8]. And D. Chen et al. showed that as extruded Mg-7Sn alloy has high ultimate tensile strength of 255 Mpa, it increases by 120% compared to as-cast alloys [9].

In addition alloying elements such as Zn [10-12] and Al [13-16] are known to have a beneficial effect on the mechanical properties of extruded Mg alloys. Extruded Mg-Sn-Zn alloys enhanced the room-temperature tensile and creep properties by solution heat-treatment and artificial aging due to the uniform dispersion of Mg₂Sn and MgZn₂ phase in the coarse grains [11]. The large amount of fine particles consisting of Mg₂Sn and MgZn phases would be responsible for the better comprehensive mechanical properties as well as a lower degree of yield asymmetry [12]. T.T. Sasaki et al. reported on a new Mg-Sn-Zn-Al-based alloy which is suitable for extrusion and has a high-strength. The extruded alloy exhibited high yield strengths of 308 MPa in tension and 280 MPa in compression, to give a tension to compression ratio of 0.9 [13]. And S.S. Park et al. reported that low-temperature superplasticity was found in the alloy, which exhibited tensile elongations of 410–950% at strain rates in the range 1×10^{-3} – 1×10^{-4} s⁻¹ at 473 K. The superplastic deformation behavior was attributed to the fine-grained microstructure, which contained thermally stable Mg₂Sn precipitates [16].

As mentioned above [2], magnesium and magnesium alloys are not attractive from the point of view of their corrosion properties. The corrosion examination of developed magnesium alloys is necessary for commercialization. So far, the corrosion research on Mg-Sn-based alloys has rarely been conducted whereas the mechanical properties of its alloy systems have been researched heavily. The corrosion properties of Mg-Sn binary alloy and Mg-Sn-Zn ternary alloy primarily depended on the amount of Mg₂Sn intermetallics, which promoted passivity and notably increased the H₂ evolution rate, and functioned as pitting corrosion initiation sites [17,18]. However, the investigation of the corrosion properties of Mg-Sn-Zn-Al has not been fulfilled. Therefore, it is difficult to determine whether Mg-Sn-Zn-Al alloy is suitable as a commercial magnesium alloy, although Mg-Sn-Zn-Al alloys have excellent mechanical properties,

Thus, in this study, the microstructure and corrosion properties of the extruded Mg-8Sn-1Zn alloy were investigated through the addition of Al alloying element.

1.2. Mn alloying element

Manganese is one of the widely used alloying element in magnesium alloys. It has been reported that the addition of manganese in magnesium alloys can refine the grain size, improve the tensile strength and enhance the fatigue life of extruded AZ61 [19], AZ31 [20] and AZ21 [21] alloys.

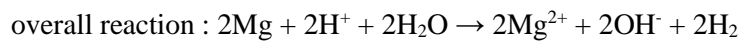
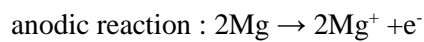
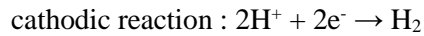
Manganese, in particularly, has a positive effect for improving the corrosion properties of magnesium alloys. Song et al. reported that the role of the Mn addition in the AZ series alloys is considered to be the transformation of iron (Fe) and other impurities into harmless intermetallic compounds [22]. X. Gu et al. reported that manganese improves the corrosion properties of pure magnesium [23]. And N.D. Nam found that high contents of manganese can accelerate the corrosion in Mg-Al alloys due to Al-Mn second particles, whereas the corrosion improving effect of manganese under 1wt% contents is approved [24].

To summarize, the small amount of manganese on a particular magnesium and magnesium alloy such as Mg-Al, or Mg-Al-Zn leads to better corrosion properties. Therefore, the manganese is also considered for improving the corrosion properties of Mg-Sn-based alloys in this study.

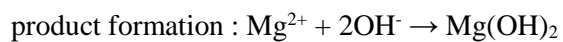
II. Theoretical review

2.1. Corrosion of magnesium

Magnesium dissolution is accompanied by H₂ evolution



The pH is increased as the result of overall reaction. It enables the formation of a hydroxide film on magnesium through following the reaction



2.1.1. Pourbaix diagram

The magnesium has a standard reduction potential of -2.37V at 25 degree Celsius. And the actual reduction potential of magnesium is about -1.7V. The reason for this difference is contact between the magnesium metal and a solution. Magnesium metal is not contact to magnesium divalent ion in solution because it forms a hydroxide film.

Hydroxide film on magnesium slightly protects the bare metal over the pH range. The Pourbaix diagram shows the thermodynamics of oxide film formation. In the case of magnesium metal, magnesium divalent ion is stable up to pH 10, and the oxide film, Mg(OH)₂, is stable above pH 10.

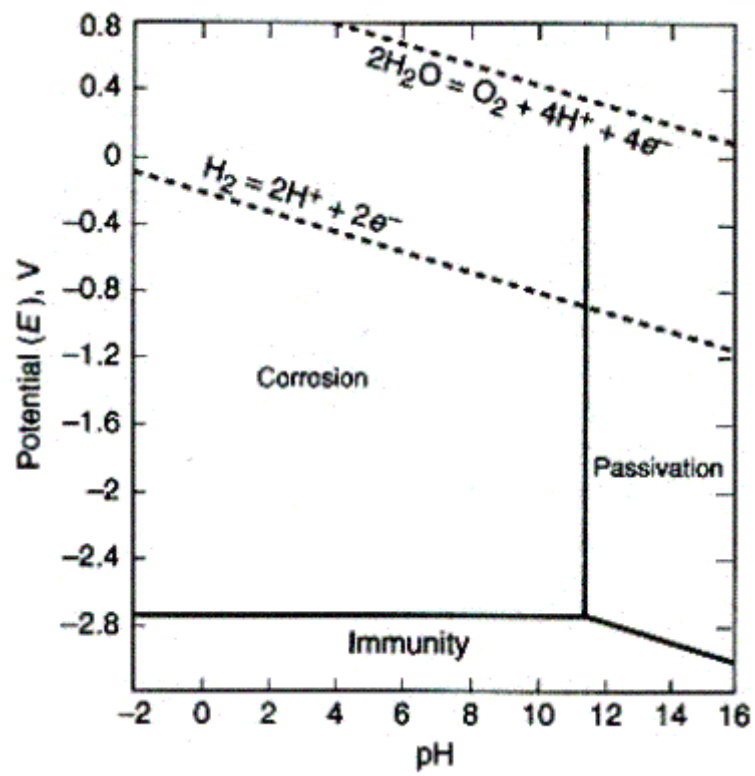


Fig. 1. Potential-pH (Pourbaix) diagram for magnesium in 25 degree Celsius water.

2.2. Corrosion mechanism of magnesium

2.2.1. Galvanic corrosion

- Macro-galvanic corrosion

Table 1. shows that many engineering metals are more noble than magnesium and magnesium alloys, so magnesium is favored to be an anode which preferentially oxidizes in galvanic couple. Therefore, the research to prevent galvanic corrosion is important to some applications that uses magnesium alloys.

Metal	E_{corr}
Mg	-1.65
Zn	-1.02
Al-7075	-0.88
Al-1xxx	-0.73
Fe	-0.50
Cu	-0.12
Ni	+0.01

Table 1. Corrosion potential of engineering metals.

- Micro-galvanic corrosion

Second particles have a considerable influence on magnesium corrosion, so second particles are very important. By similar principle of micro-galvanic corrosion, magnesium matrix is favored to be an anode which preferentially oxidizes in a galvanic couple. The cathodes can be second particles or impurities. The schematic diagram of micro-galvanic is shown in Fig. 2. And the corrosion potential of magnesium and its second particles is in Table 2 [25,26]. The corrosion rate of magnesium and its alloys at E_{corr} is in Table 3 [27]. Table 3 clearly shows the mechanism of galvanic corrosion. The magnesium matrix acts as anode and the second particles act as cathode.

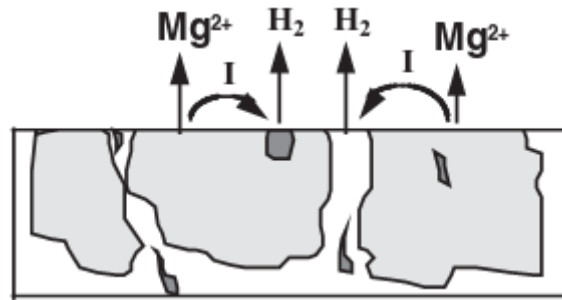


Fig. 2. Schematic diagram of micro-galvanic corrosion.

Metal	E_{corr}
Mg	-1.65
Mg ₂ Si	-1.65
Al ₆ Mn	-1.52
Al ₄ Mn	-1.45
Al ₈ Mn ₅	-1.25
Mg ₁₇ Al ₁₂ (β)	-1.20
Al ₈ Mn ₅ (Fe)	-1.20
Beta-Mn	-1.17
Al ₄ MM	-1.15
Al ₆ Mn (Fe)	-1.10
Al ₆ (Fe)	-1.00
Al ₃ Fe (Mn)	-0.95
Al ₃ Fe	-0.74

Table 2. Corrosion potential of magnesium and second particles in 5% NaCl solution (pH 10.5) [26].

Sample	Rate[mm/y]	Mechanism
LP MG (240 ppm Fe)	53	Impurity accelerated corrosion
HP AZ91 sand cast	12	β accelerates corrosion
AZ91D – die cast (interior)	5.7	β accelerates corrosion
High purity Mg	1.1	Standard for comparison
AZ91D – di cast (surface)	0.66	β protects
β Phase	0.30	
The Z-phase	10^{-6}	Needs to be more passive than the β phase and have a lower ability to liberate hydrogen on its surface

Table 3. Corrosion rates at E_{corr} in 1N NaCl solution [27].

2.2.2. Localized corrosion

The common form of magnesium corrosion is localized corrosion. Localized corrosion is initiated from some pits which are selectively attacked, because magnesium and its alloys have a partial protective film.

- Pitting corrosion

Small cavities, second particles, and impurities can be the initiation site for corrosion. These are called pits. Some pits and, small cavities, which are selectively attacked become anodic sites and the magnesium matrix become cathodic sites. The galvanic couple between pits and matrix is produced, then galvanic corrosion occurs in a small, limited area.

Fig. 3 shows the pitting corrosion mechanism of AM60 alloy [28]. It seems to be initiated from second particle, AlMn. The specific step of pitting corrosion on AM60 alloy is that it has a protective oxide film in the air at first. And Cl^- ions absorb on the magnesium matrix bordering on AlMn particles during immersion in NaCl solution. If the potential of the oxide later reaches to its free corrosion potential ($P_{\text{corr}} = -1.53\text{V}$ for AM60), the magnesium matrix and AlMn particles makes a galvanic couple and start to dissolve. A corrosion nucleus may then form nearby an AlMn particle causing it to develop into a corrosion pit. This process may result in $\text{Mg}(\text{OH})_2$ formation and hydrogen evolution according to the corrosion reactions. A hemi-spherical corrosion pit forms with the corrosion proceeding. The pH value will finally reach and stay in an alkaline condition due to the formation of $\text{Mg}(\text{OH})_2$.

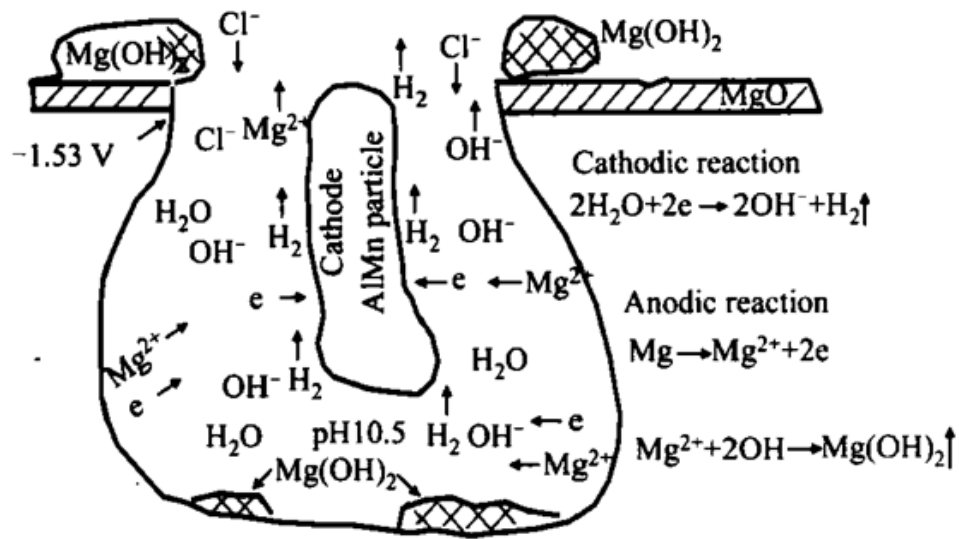


Fig. 3. Schematic diagram of pitting corrosion for AM60 alloy.

- Filiform corrosion

Filiform corrosion usually appears on the coated or anodized surfaces and requires the presence of a coating which is resistant to the corrosive environment. The filaments propagation is driven by the oxygen reduction reaction at the cathodic sites [29]. However, the filiform corrosion has already been observed on the bare magnesium and its alloys in various solutions. Schmutz et al. [30] reported that pure magnesium was susceptible to localized corrosion in the form of filaments in a solution containing both chloride and dichromate ions. O. Lunder et al. [31] found that the early stage corrosion of AZ91 alloy in 5% NaCl solution was characterized by filiform corrosion. They both agreed that there was a protective surface film covering the magnesium substrate and the cathodic reaction of filiform corrosion was driven by hydrogen evolution.

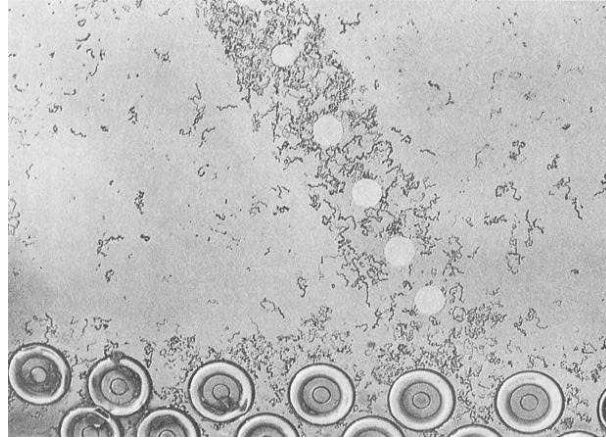


Fig. 4. Image of filiform corrosion.

2.2.3. Intergranular corrosion

Intergranular corrosion is produced along the grain boundaries due to the precipitation of the second phase. A Grain boundary is the preferred position at which precipitation can occur. Although there are some arguments about the intergranular corrosion of magnesium, it is observed that the intergranular corrosion can occur in magnesium and its alloys [32-33]. T. Valente et al. noticed that the grain boundaries suffered preferred attacks, and intergranular corrosion occurred for WE43 in 3.5% NaCl aqueous solution [32]. E. Ghali et al. also pointed out that in the early stages of immersion, a localized attack of Mg and its alloy can be formed at the grain boundaries at the interface of cathodic precipitates in mild corrosive media. These can be considered as intergranular corrosion [33].

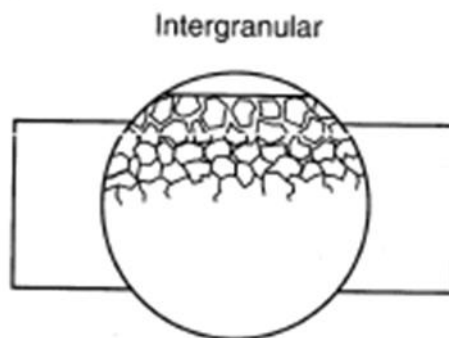


Fig. 5. Schematic diagram of intergranular corrosion.

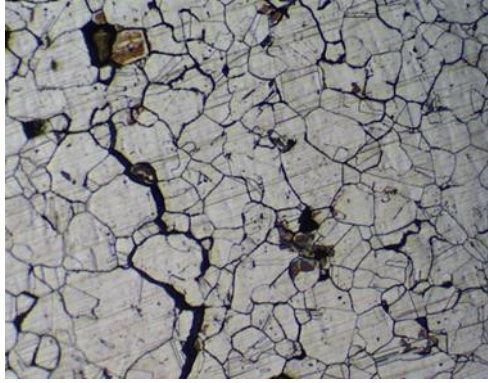


Fig. 6. Image of intergranular corrosion.

2.2.4. Environment cracking

Environmental cracking is a corrosion that occurs due to environmental factors.

- Stress Corrosion Cracking (SCC)
- Corrosion fatigue

2.3. Material factors affecting corrosion of magnesium

2.3.1. Alloying elements [34]

Al, Ca and, Mn are the most common alloying elements of magnesium and its alloys. These alloying elements make the second particles, intermetallic phases. Second particles have an influence on microstructure, mechanical properties and corrosion properties.

- ✓ Alloying elements which improve the corrosion properties : Mn, Er, Ce, La, Nd
- ✓ Influence on the corrosion properties depends on contents of alloying element : Ca, Zn, Zr, Sr (when the content is high, the corrosion resistance deteriorates, whilst when the content is low, they slow the corrosion rate of the Mg alloys.)
- ✓ Alloying elements which reduces the corrosion properties : Li
- ✓ The effect of alloying elements is not well understood : Gd, Y

The research on the alloying elements effect is considerably significant for developing new magnesium alloys. The detailed influence of each alloying elements is shown in Table 4 and Table 5 [34]. Fig. 7 shows the change of E_{corr} by adding various elements on AZ91 alloys. Fig. 8 also shows the change of I_{corr} by adding various elements on AZ91 alloys [35].

Elements	Effects on the microstructure	Effects on mechanical properties	Effect on corrosion resistance	References
Al	Refinement of grain size; reaction with Mg to form the $Mg_{17}Al_{12}$ phase; high Al concentration leads to a network distribution of $Mg_{17}Al_{12}$ along grain boundaries	Enhances castability and hardness; increases yield strength at a concentration above 3%; significantly improves ultimate yield strength and ductility at a concentration below 6%	A network distribution of $Mg_{17}Al_{12}$ in Mg alloys enhances corrosion resistance; however, the coupled micro-galvanic effects between the $Mg_{17}Al_{12}$ phase and Mg matrix at the same time increase the corrosion rate	2, 18–32, 75, 91, 97 and 101–109
Ca	Reduction of the grain size with the addition of Ca below 15% in binary Mg–Ca alloys; formation of Mg–Ca phases distributed along the grain boundaries	Increases elasticity; compressive yield strength; ultimate strength and hardness with increasing Ca content less than 20%; increases the creep properties at a concentration less than 0.3%; deteriorates ductility at a concentration from 0.5 to 15%	Excessive addition of Ca in pure Mg deteriorates corrosion resistance; Ca concentration in Mg alloys should be less than 1%	45, 48, 54, 55, 58, 59, 61, 64–67, 101 and 110
Li	Slightly decreases the grain size; Mg–Li phases with a bcc structure distribute along grain boundaries	Increases deformability with high addition (>11%) by forming bcc structural phases; decreases the strength significantly	Enhances corrosion resistance at a concentration below 9% in pure Mg; accelerates the corrosion rate significantly with higher Li addition	13, 30, 34, 86, 101, 111, 112 and 114
Mn	Significant grain refining at low Mn concentration in Mg–Al based alloys; removes impurities by forming new phases with Fe and other heavy metals	Slightly increases the yield strength; decreases the ultimate yield strength and elongation for binary Mg–Mn alloys; the effect on mechanical properties is dependent on the composition of Mg alloys; rarely used in pure Mg	Enhances corrosion resistance by reducing impurities with a small quantity of Mn addition	5, 43–45, 68, 101 and 115–119
Zn	No obvious effect on grain refining with the addition below 5% for binary Mg–Zn alloys; reacts with Mg to form a secondary phase and distributes along grain boundaries; usually used with Al in Mg alloys	Enhances the tensile strength; excellent solid solution strengthening and aging strengthening; deteriorates castability at high concentrations; reduces the influences of Ni and Fe	Inhibits the harmful effects of Fe and Ni impurities on the corrosion; enhances the corrosion resistance of Mg alloys at a content below 5%	5, 40, 41, 43–48, 63, 68, 95, 96, 101 and 120–123
Zr	Excellent grain refining; extremely low solid solubility in pure Mg; using with Al in Mg alloys should be avoided due to the formation of the stable Al–Zr phase that deteriorates the mechanical properties	Slightly increases the ultimate compressive strength with increasing Zn concentration; significantly enhances the ductility, elongation and ultimate yield strength of Mg alloys with a small amount of addition in binary Mg–Zr alloys; usually used with Zn in Mg alloys	Small amounts of Zr addition (less than 2%) enhances the corrosion resistance; otherwise significantly deteriorates the corrosion resistance	36, 52, 53, 56, 57, 101, 102, 124, 125 and 128
Sr	Refinement of grain size; leads to rough boundaries with excessive addition; reacts with Mg to form Mg–Sr phases that distribute along grain boundaries	Increases the tensile strength with the Sr addition below 2%; decreases ultimate strain and ultimate compressive strength due to the superabundant compounds in grain boundaries	The influence on corrosion depends on the fraction volume of $Mg_{17}Sr_2$ phases in Mg alloys, optimal content less 2%	56, 64, 72–75 and 130

Table 4. Influence of alloying elements on magnesium alloys [34].

Elements	Effects on the microstructure	Effects on mechanical properties	Effect on corrosion resistance	References
Ce	Excellent grain refining for pure Mg and AZ alloys; Mg-Ce phases isolate the Mg matrix and reduce the grain size; Al-Ce phases distribute along grain boundaries; excessive Ce addition to Mg leads to the formation of brittle Mg-Ce phases distributing along grain boundaries	Enhances tensile strength and tensile yield strength with the addition of Ce below 6% for binary Mg-Ce alloys; however tensile yield strength remains stable and tensile strength decreases with increasing addition of Ce after T6 treatment; deteriorates the elongation of Mg alloys with excessive addition of Ce; deteriorates creep resistance; enhances the tensile strength of AZ alloys with 1% Ce addition	Formation of the $Al_{13}Ce_3$ phase surrounding the Mg matrix in AZ alloys, suppressive galvanic effects and thus enhancement of corrosion resistance; however, increasing addition of Ce deteriorates the corrosion resistance of binary Mg-Ce alloys due to the galvanic effect	113, 127, 129-137, 140 and 143
Er	Exhibits low solubility in solid Mg; forms stable Mg-Er phases; Er addition to Mg-Al alloys leads to the formation of an Al-Er phase; excellent grain refining in ZK alloys	Improves tensile strength and tensile yield strength with the increasing addition of Er to pure Mg; however it decreases the elongation of Mg-Er alloys	Enhances the corrosion resistance of AZ alloys; Mg-Al-Er phases surround the Mg matrix; enhances the stability of the $Mg(OH)_2$ layer and thus reduces corrosion resistance	113 and 138-144
Gd	Refinement of grain size; Gd atoms replace Mg atoms to form a random substitutional solid solution	Enhance tensile strength and tensile yield strength with the increasing addition of Gd; improve the elongation of Mg-Gd alloys with the addition of Gd below 6%	No consensus. Influence on corrosion depends on the composition and Gd content in Mg alloys	113, 128, 141 and 145-151
La	Has a relatively low solubility in Mg compared with other rare earth elements; reacts with Al to form rod-like Al-La phases that refine the grain size of AZ alloys	Enhances tensile strength, yield strength and creep resistance of binary Mg-La alloys; deteriorates the elongation of Mg alloys with excessive addition of La; reduces dendrite arm spacing and slightly improves the tensile strength and age hardening response of Mg-Al-La alloys due to the formation of Al-La phases	Refinement of $Mg_{17}La_2$ phases leading to a finer microstructure for Mg-La alloys with La addition below 1%, which results in uniform corrosion; La oxide combined with $Mg(OH)_2$ enhances corrosion resistance	113, 129, 131 and 152-154
Nd	Refinement of the grain size of Mg alloys with increasing Nd content	Nd atoms replace Mg atoms thereby enhancing the tensile strength and tensile yield strength at a Nd content less than 6%; deteriorates elongation and creep resistance of Mg alloys with excessive addition of Nd	Addition to pure Mg effectively enhances corrosion resistance; the $Mg_{12}Nd$ phase suppresses the galvanic effect; the Nd_2O_3 layer combined with $Mg(OH)_2$ inhibits corrosion	113, 133, 155 and 156
Y	Excellent grain refining; relatively high solid solubility in Mg; always used with other REEs to enhance creep resistance of Mg alloys due to the formation of Y-rich phases	Significantly enhances tensile strength and tensile yield strength with increasing addition of Y in pure Mg; improves elongation with the Y concentration below 3%; excessive addition of Y deteriorates elongation	Influence on corrosion resistance under debate; depends on the composition of Mg alloys; reduces corrosion resistance of binary Mg-Y alloys with a concentration >2%	38, 46, 49, 61, 93, 113, 154 and 158-161

Table 5. Influence of alloying elements on magnesium alloys (2) [34].

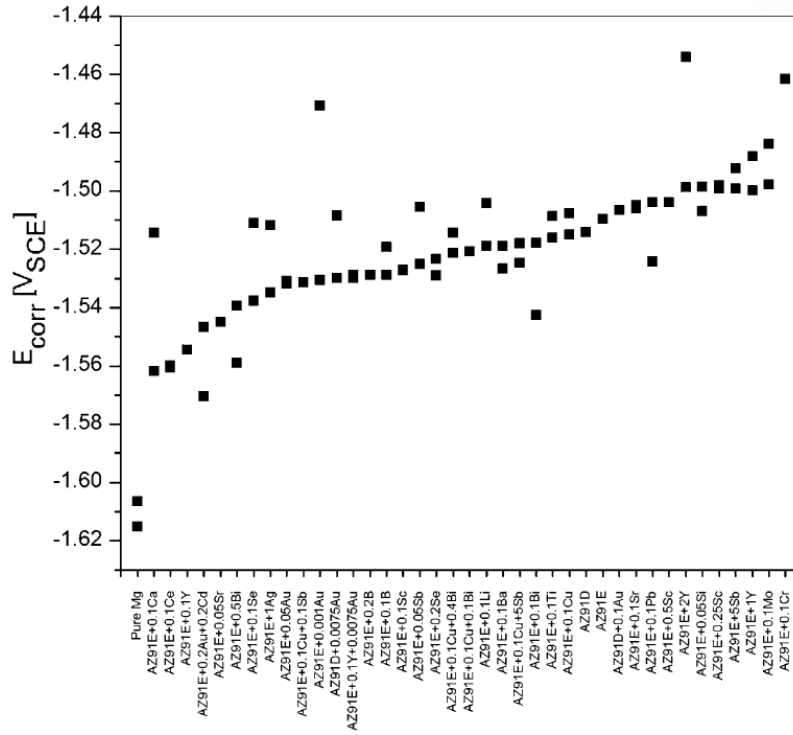


Fig. 7. Influence E_{corr} by adding various elements on AZ91 alloy.

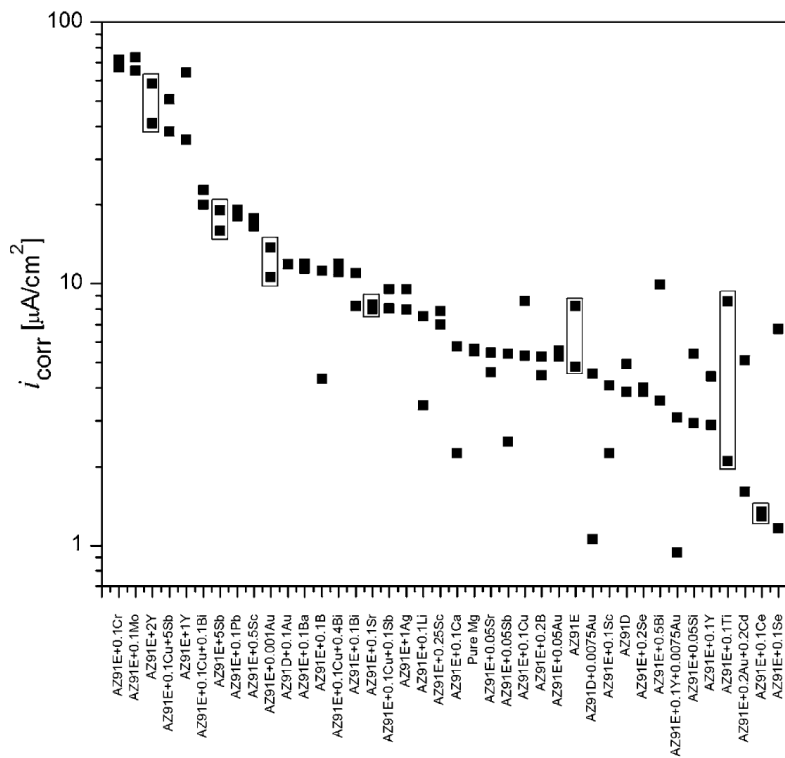


Fig. 8. Influence I_{corr} by adding various elements on AZ91 alloy [35].

2.3.2. Purity

Purity is a critical factor that can determine the corrosion properties of magnesium and its alloys. Some contaminants such as iron, nickel, and copper accelerate the corrosion rate by over ten times. There are two major reasons that iron, nickel and copper have negative effects on corrosion behavior. One is their low solid solubility, and the other is the active nature as cathodic sites. Among them, the impact on corrosion behavior of nickel is the greatest and copper effect is the lowest, not considering the concentration factor. Each contamination which accelerates the corrosion has its permitted limit. The corrosion behavior remains as they were under its permitted limit. But over its permitted limit, the corrosion behavior deteriorates, because the contaminants like iron, nickel, and copper act as catalysts for initiating the corrosion [36].

Therefore, the concentration of contaminants is fixed for good corrosion performance. In the case of AZ91 alloy, specific concentrations of contaminants include the following; Fe < 50 ppm, Ni < 5 ppm, Cu < 300 ppm.

2.4. Evaluation of corrosion behavior

There are various corrosion evaluation methods. Through some corrosion experiments, we can calculate the corrosion rate. This enables us to evaluate and compare the corrosion performance of materials.

2.4.1. Immersion test [37]

One of the corrosion evaluation methods, the immersion test is the most general and economical. The specimen for evaluation is immersed in enough solution (over 0.2mL mm²) for a certain period. After the immersion test, the corrosion produce can be removed by cyclic cleaning in 180g L⁻¹ chromic acid. The corrosion rate can be calculated by considering the weight loss of the sample, the exposure time, exposure area, and the density of the specimen.

$$\text{Corrosion Rate} = (K \times W) / (A \times T \times D)$$

Where K = a constant,

T = time of exposure in hours,

A = area in cm²,

W = mass loss in grams, and

D = density in g/cm³

Corrosion Rate Units	Constant (K)
mils per year (mpy)	3.45×10^6
inches per year (ipy)	3.45×10^3
inches per month (ipm)	2.87×10^2
millimeters per year (mm/y)	8.76×10^4
micrometers per year (μm/y)	8.76×10^7
picometers per second (pm/s)	2.78×10^6
grams per square meter per hour (g/m ² ·h)	$1.00 \times 10^4 \times D$
milligrams per square decimeter per day (mdd)	$2.40 \times 10^6 \times D$
micrograms per square meter per second (μg/m ² ·s)	$2.78 \times 10^6 \times D$

Table 6. The constants (K) in corrosion rate equation [37].

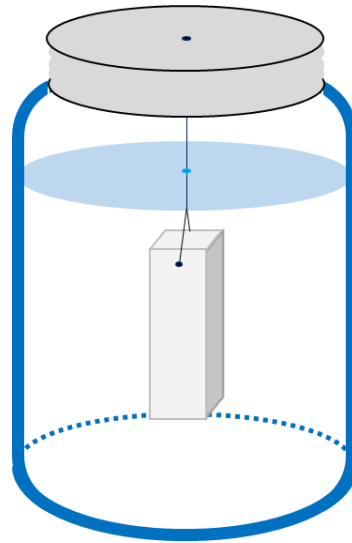


Fig. 9. Schematic diagram of immersion test.

2.4.2. Potentiodynamic test [38,39]

The potentiodynamic test can evaluate the corrosion properties much faster than the immersion test. The applied potential in this test determines the direction of reaction, anodic or cathodic. The current can express the corrosion rate of reaction.

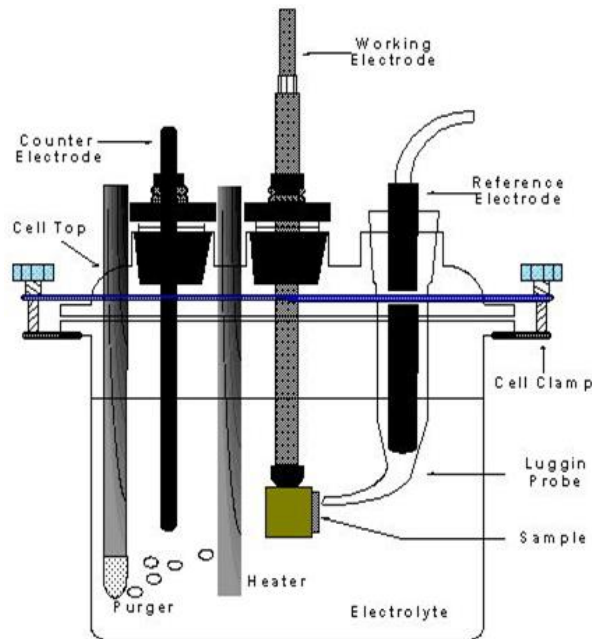


Fig. 10. Schematic diagram of 3-electrode cell which uses for potentiodynamic test.

The corrosion behavior is usually evaluated by the polarization technique. The following equation is about the polarization technique, and is related to i_{app} and E_{app} .

$$i_{app} = i_{corr} \left[\exp \frac{2.3(E - E_{corr})}{\beta_a} - \exp \frac{-2.3(E - E_{corr})}{\beta_c} \right] + C \frac{dE}{dt}$$

where i_{app} : applied current density,

i_{corr} : corrosion current density,

E : applied voltage,

E_{corr} : open circuit potential,

C : interfacial capacitance associated with β_a and β_c ,

β_a and β_c : Tafel coefficients, slope of anodic and cathodic reaction, and

dE/dt : scan rate

When the overpotential (η) is measured, the following equations can be used.

$$\eta_a = \beta_a \log \frac{i_{app}}{i_{corr}} \quad , \quad \eta_c = -\beta_c \log \frac{i_{app}}{i_{corr}}$$

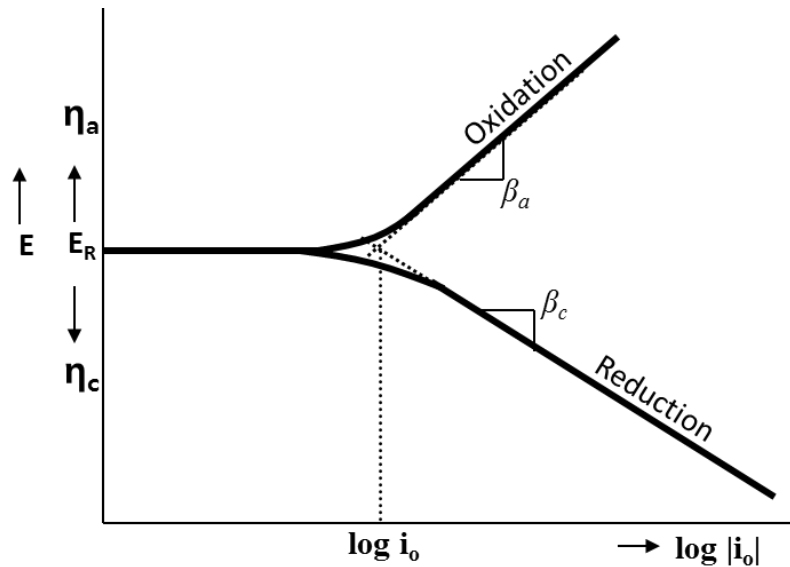


Fig. 11. Polarization curve.

2.4.3. Others

- H₂ evolution test

Generally the oxidation of magnesium alloy coincides with the reduction of hydrogen. So, active reduction means that corrosion of magnesium is accelerated. The corrosion rate can be evaluated and compared by measuring the amount of hydrogen evolution

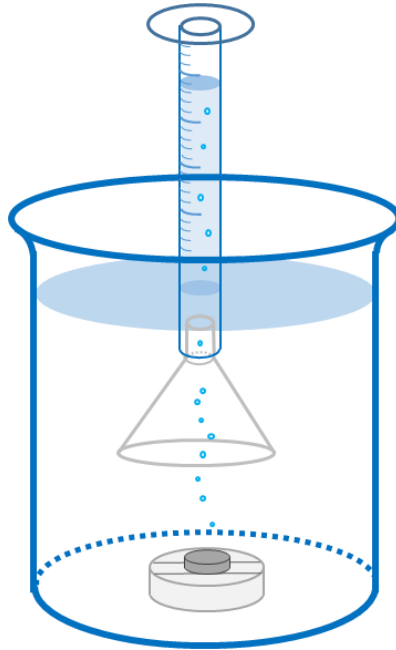


Fig. 12. Schematic diagram of hydrogen evolution test [40].

- Salt spray test

The Salt spray test evaluates the corrosion behavior by the weight loss method.

III. Influence of Al addition

3.1. Introduction

As mentioned, the corrosion research on Mg-Sn-based alloy has rarely been conducted whereas the mechanical properties of its alloy system have been heavily researched. The corrosion research on Mg-Sn-Zn-Al alloy is not investigated, even though its alloy has outstanding strength and superplasticity. In this study, therefore, high-strength Mg-8Sn-1Zn alloys with different Al contents were subjected to indirect extrusion, and the effects of Al content on the microstructure and corrosion properties of the extruded alloys were investigated. This study aims to assess the suitability of Mg-Sn-Zn-Al alloy as a commercial magnesium alloy.

The microstructure is analyzed with OM, XRD, SEM, TEM. The corrosion properties are evaluated by immersion tests, potential monitoring, and potentiodynamic tests. The potential of intermetallic is analyzed by SKPFM.

3.2. Experimental

3.2.1. Sample preparation

The analyzed compositions of the Mg–8Sn–1Zn-based alloys used in this study are given in Table 1. Extrusion billets were prepared by induction melting in a graphite crucible under an inert atmosphere with a CO₂ and SF₆ mixture, and subsequent pouring into a steel mould pre-heated to 200 °C. Cast billets were homogenized at 500 °C for 3 hours and then water-quenched. The billets were 80 mm in diameter and 200 mm in length. Indirect extrusion experiments were implemented with an initial billet temperature of 250 °C, a ram speed of 1.3 mm s⁻¹, and an extrusion ratio of 25.

3.2.2. Microstructure characterization

Microstructural examinations were conducted on the midsections of the extruded samples perpendicular to the extrusion direction (ED). Each sample was ground on SiC papers up to 2000 grit under water atmosphere, and then polished using 1 μm diamond paste and 0.04 μm colloidal silica solution under ethanol atmosphere, respectively. The polished samples were chemically etched to reveal grain boundaries using a solution consisting of 10 ml acetic acid, 4.2 g picric acid, 10 ml distilled water, and 70 ml ethanol. Microstructures were observed using a Nikon EPIPHOT 200 optical microscope, a Quanta 200 field-emission scanning electron microscope (SEM) equipped with an energy dispersive spectrometer (EDS), and a JEM-2100F Cs-corrected transmission electron microscope (TEM) equipped with EDS. Grain size was measured using a linear intercept method, $d=1.74 \times L$, where d is the grain size and L is the linear intercept size. The volume fraction of precipitated particles was determined by measuring the area fraction of the particles. The grain sizes and particle volume fractions were averaged from values measured from four optical and SEM micrographs for every alloy, respectively. TEM samples were fabricated using a focused ion beam (FIB) technique. X-ray diffraction (XRD) analyses were conducted with a Rigaku D/MAX-2500/PC in the back reflection mode with Cu-K α radiation.

3.2.3. Electrochemical and immersion tests

The corrosion behavior of the extruded alloys was investigated using immersion tests, corrosion potential (E_{corr}) measurements, and potentiodynamic polarization tests at room temperature. The electrochemical tests were conducted at two concentrations of NaCl, 0.005 and 0.6 M, in order to obtain clear results as well as to confirm reproducibility. The solution for the potentiodynamic polarization tests was deaerated by N_2 purging throughout testing. Prior to the immersion test, the alloy samples were mechanically ground using SiC papers up to 2000 grit. After immersion for 72 hours in 0.6 M NaCl solution the samples were cleaned with 200 g l^{-1} CrO_3 solution and then the weight loss of the samples was measured.

For the electrochemical tests, a conventional three-electrode cell comprising a working electrode (sample), a saturated calomel reference electrode (SCE) and a Pt plate counter electrode was used; the electrochemical tests were conducted using a potentiostat (Reference 600, GAMRY, USA). The samples were ground using SiC papers up to 2000 grit, and an exposed area of 0.13 cm^2 was delineated using electroplating tape. The polarization test was conducted at a scan rate of 1 or 2 mV s^{-1} , and the potential scan started at -0.3 V versus E_{corr} level to each pitting potential (E_{pit}) level of the samples. All electrochemical tests were conducted at least three times to confirm reproducibility.

3.2.4. Scanning Kelvin probe force microscopy

To measure the relative Volta potential differences between second-phase particles and the α -Mg matrix, the potential galvanic interactions between these phases were examined by means of scanning Kelvin probe force microscopy (SKPFM) (XE-70, Park Systems). All of the measurements were performed at room temperature under a controlled relative humidity of $40 \pm 5\%$. The Au/Cr-coated conducting tip was modulated by AC modulation of 1.5 V (rms) at frequencies of 17–18 kHz using an external lock-in amplifier (SR-830, Stanford Research Systems). The contact potential difference was obtained by adding a DC feedback voltage to the sample to nullify the electrostatic force component between the tip and the sample, which is proportional to the first harmonic signal of the lock-in amplifier.

3.3. Results

3.3.1. Microstructure

Fig. 13 shows the optical micrographs of the extruded TZ and TZA alloys, which have different levels of Al content. The microstructures were found to mostly consist of α -Mg grains, which were formed by dynamic recrystallization (DRX) during extrusion. The TZA alloys, nominally containing 0.3 – 3.0wt% Al, show somewhat smaller grain sizes as compared to the TZ81 alloy, indicating that Al addition has an influence on grain refinement to some extent. However, there are no tendencies governing grain sizes according to Al contents. The grain sizes were measured to be 6.7 ± 1.0 , 4.8 ± 0.6 , 4.4 ± 0.5 , and 4.6 ± 0.4 μm , on average, for the TZ81, TZA810, TZA811, and TZA813 alloys, respectively. Fig. 13 also shows that second-phase particles are present with the α -Mg grains.

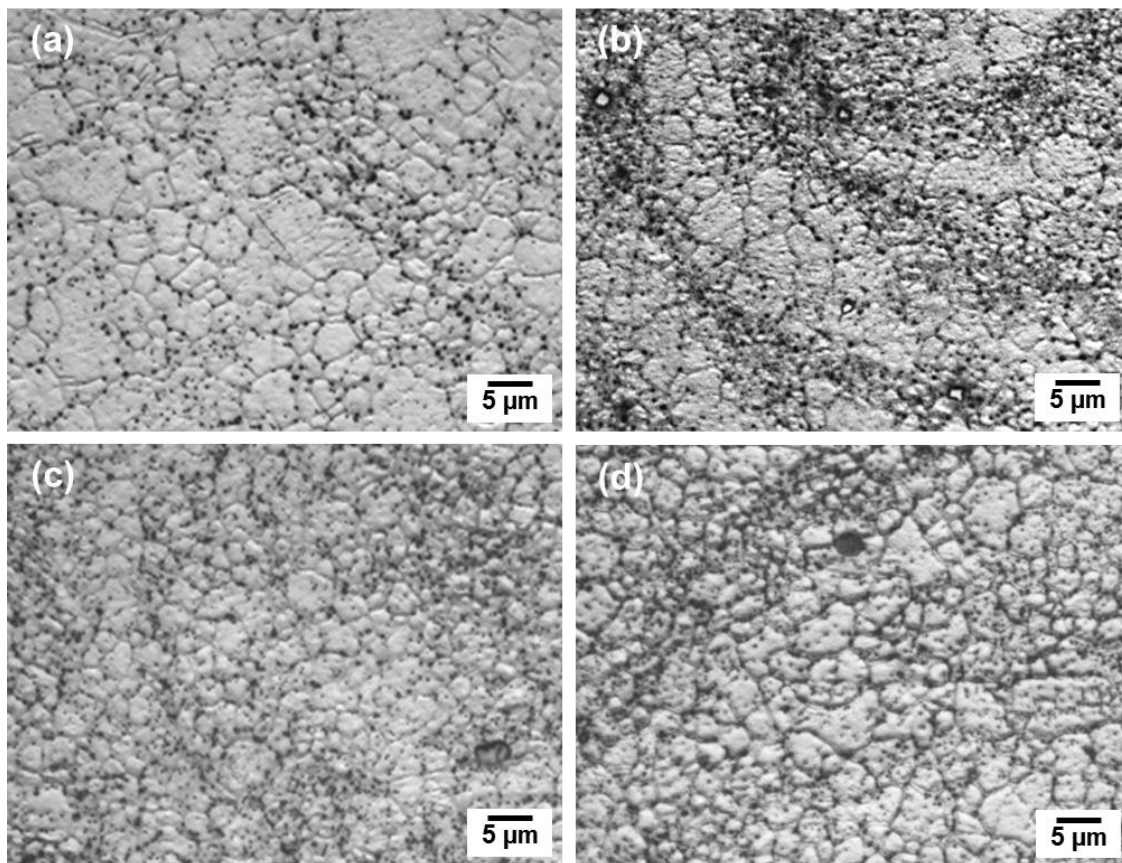


Fig. 13. Optical micrographs of the extruded alloys: (a) TZ81, (b) TZA810, (c) TZA811, and (d) TZA813.

XRD results given in Fig. 14 indicate that the main second-phase in the extruded alloys is Mg_2Sn , as typically observed in Mg-Sn-based alloys. It is reported that Mg_2Sn particles have considerable effects on mechanical properties and corrosion properties in Mg-Sn-based alloys [3-18].

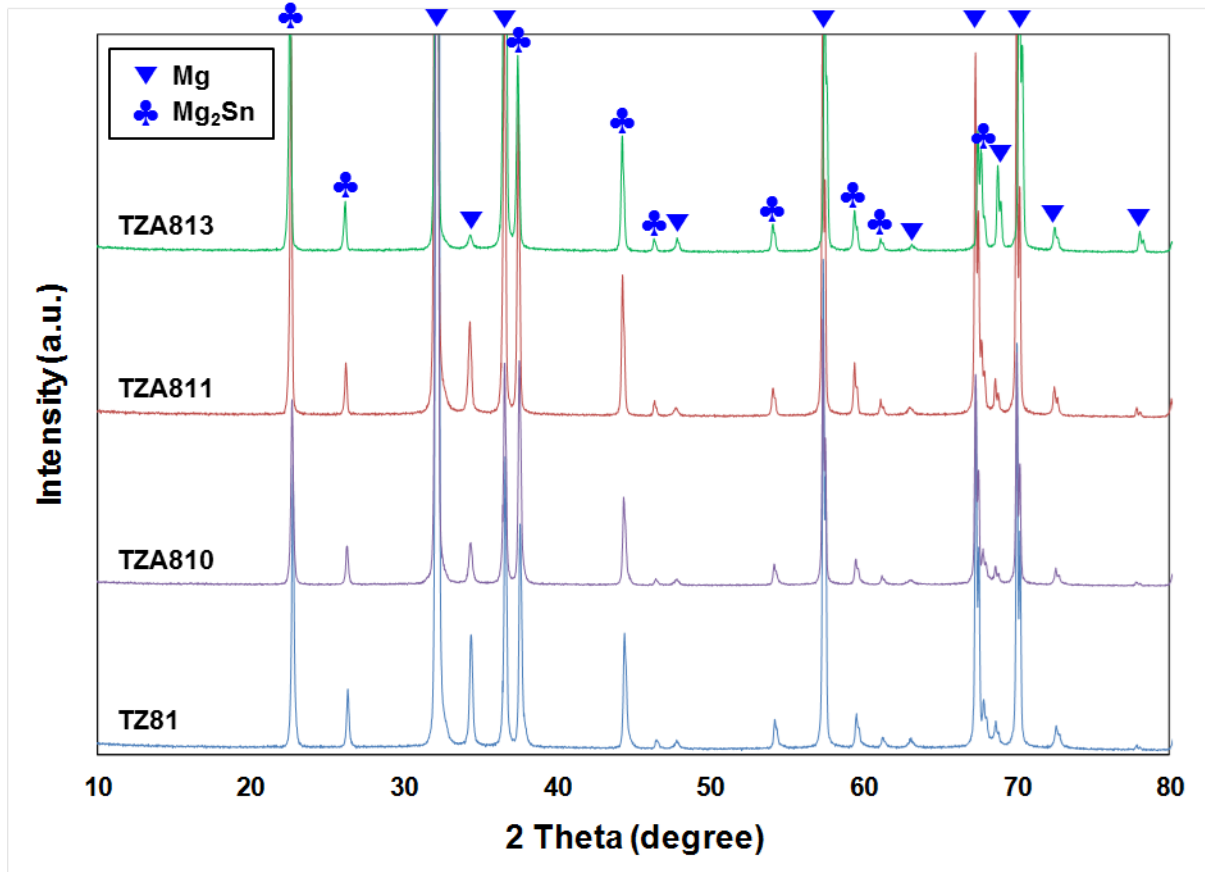


Fig. 14. XRD patterns showing the presence of Mg and Mg_2Sn phases in the extruded alloys.

SEM micrographs in Fig. 15 show that two types of Mg_2Sn particles exist in the microstructures; fine precipitates, with sizes of several hundreds of nanometers, formed via dynamic precipitation during extrusion; and relatively coarse particles formed during billet casting, which remained even after homogenization prior to extrusion. Small differences were observed in the total amount of Mg_2Sn particles among the extruded alloys, with the volume fractions being in the range of 3.4 – 3.7%.

It is hard to find the other kind of second-phase particle in TZ81 alloy. The SEM micrographs reveal that other kinds of second-phase particles, denoted as A–C in Fig. 15, are also present in the TZA alloys and the SEM micrograph.

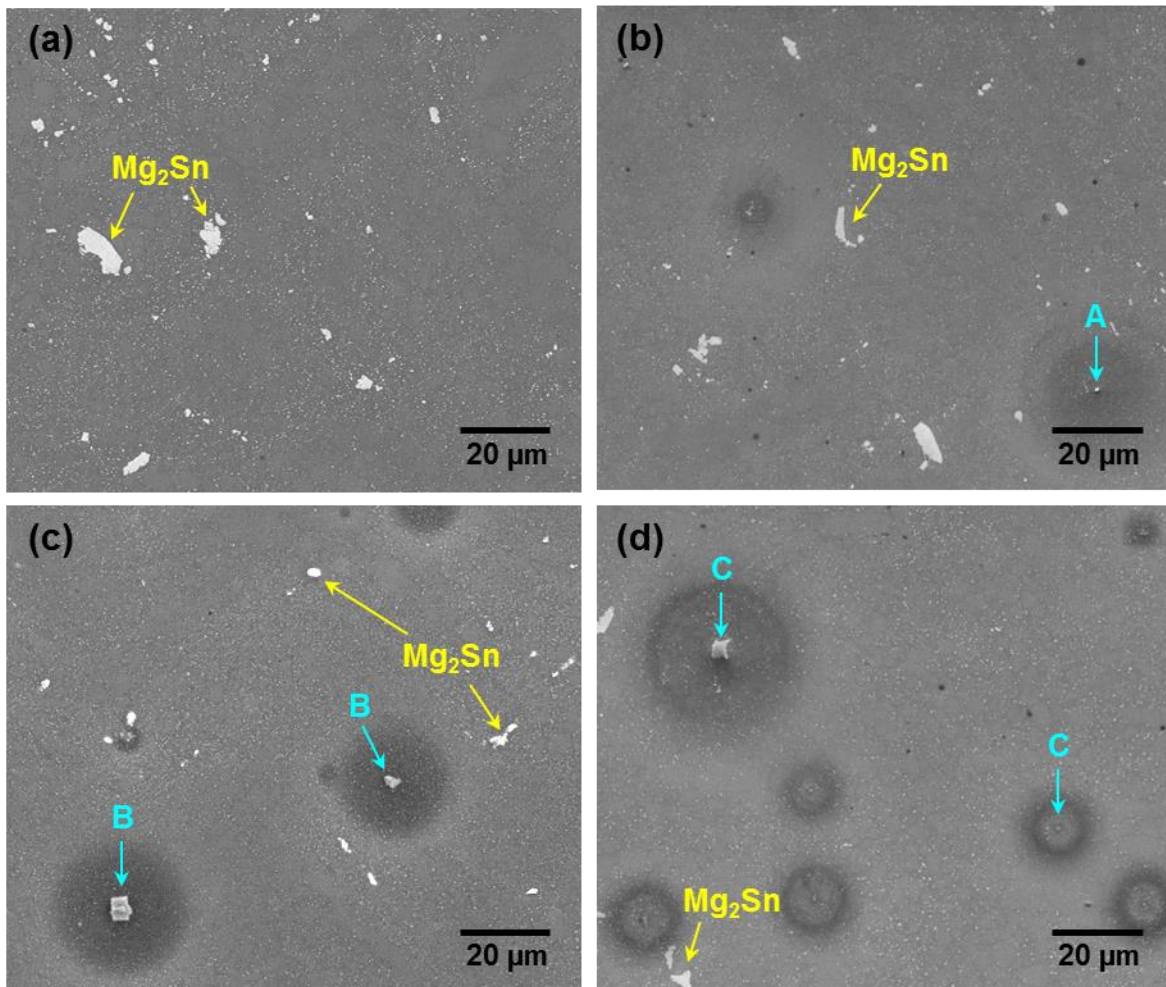


Fig. 15. SEM micrographs of the extruded alloy: (a) TZ81, (b) TZA810, (c) TZA811, and (d) TZA813. Particles labeled A–C were observed in the TZA810, TZA811, and TZA813 alloys, respectively.

These particles are more clearly observable with TEM micrographs in Fig. 16a. EDS analyses indicated that these particles mainly consist of Al and Fe, although Al/Fe ratios differed depending on compositions, as shown in Fig. 16b. The Al/Fe ratio of A particle is particularly small in TZA810 alloys which contains relatively small amount of Al. The formation of such Al-Fe particles is notable since the Fe content detected in each alloy is as small as 0.002wt%, as shown in Table 7.

Alloy	Nominal composition	Analyzed composition
TZ81	Mg-8Sn-1Zn	Mg-7.65Sn-0.99Zn
TZA810	Mg-8Sn-1Zn-0.3Al	Mg-7.58Sn-0.89Zn-0.27Al
TZA811	Mg-8Sn-1Zn-1Al	Mg-7.69Sn-0.94Zn-0.96Al
TZA813	Mg-8Sn-1Zn-3Al	Mg-7.70Sn-0.99Zn-2.76Al
Impurities	Fe \leq 0.002%, Si \leq 0.002%, Mn \leq 0.009%, Ca \leq 0.005%	

Table 7. Nominal and analyzed compositions (wt%) of the extruded alloys investigated in this study.

The Al-Fe particles in the TZA810 alloy have a small amount of Si and Mn as well. Particles containing Fe were hardly observed in the TZ81 alloy, suggesting that most of the Fe atoms in the alloy exist within the α -Mg matrix in the form of solid solution. Analyses of TEM diffraction patterns, shown in Fig. 16c, confirm that the types of Al-Fe particles differ depending on Al contents in the alloys. The Al-Fe particle in the TZA810 alloy can be identified as AlFe, which has a simple cubic structure with a lattice parameter of $a=0.290$ nm. The volume fraction of the AlFe particles was measured to be as small as $0.004\pm 0.003\%$. However, the TZA811 and TZA813 alloys have a different type of the Al-Fe particle; it can be identified as Al_5Fe_2 , which has an orthorhombic structure with lattice parameters of $a=0.765$ nm, $b=0.641$ nm, and $c=0.422$ nm. The amount of Al_5Fe_2 particles was found to be an order larger than that of AlFe particles; the volume fractions of the Al_5Fe_2 particles are 0.030 ± 0.014 and $0.037\pm 0.034\%$ for the TZA811 and TZA813 alloys, respectively.

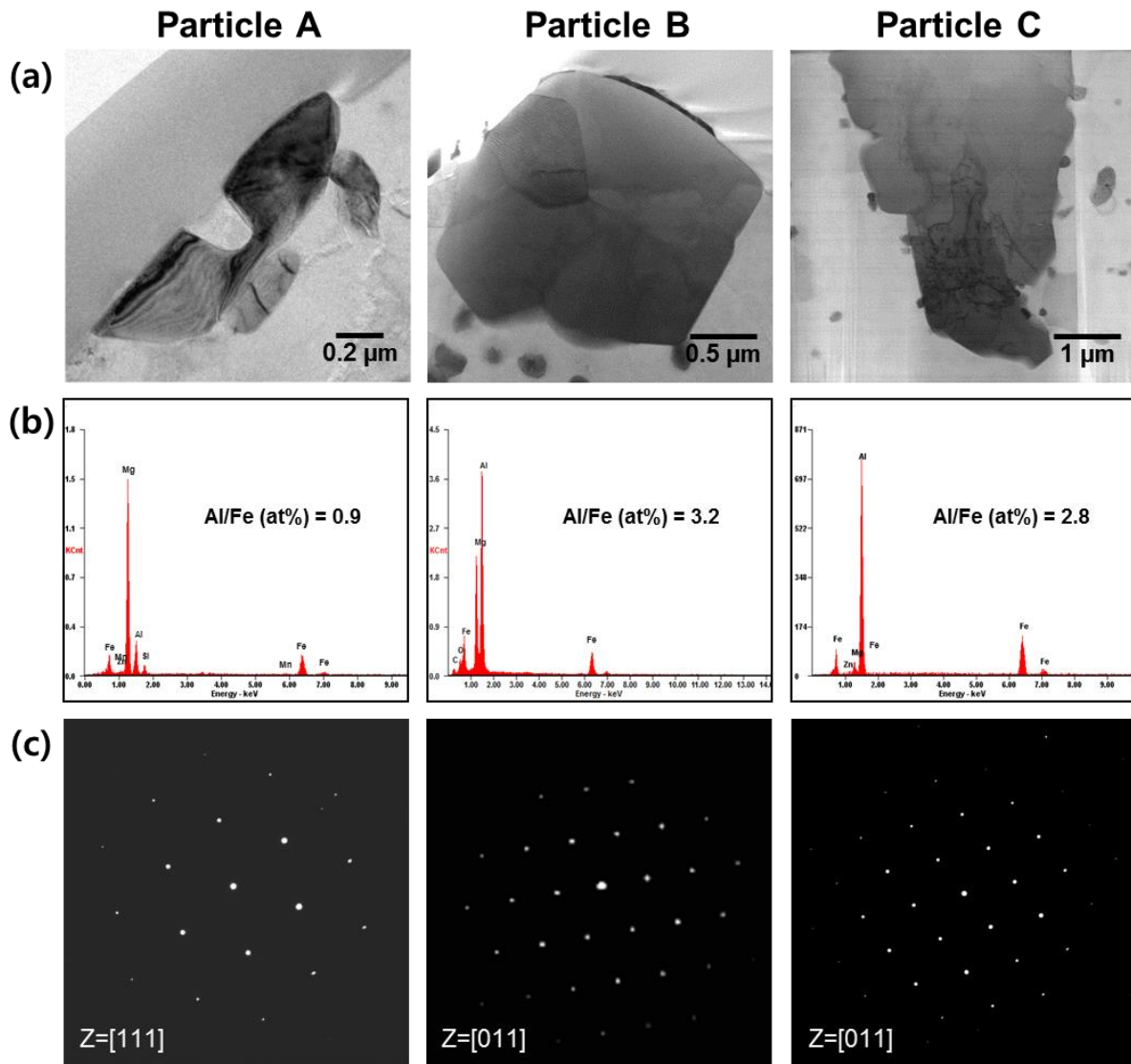


Fig. 16. (a) TEM micrographs showing the particles A-C in Fig. 15. (b) EDS spectra and (c) electron diffraction patterns from the particles.

3.3.2. Immersion test

During immersion in the 0.6 M NaCl solution, every extruded alloy exhibited spontaneous passivity under the open circuit condition, and corrosion was found to begin at points where the passivity broke, resulting in the occurrence of pitting corrosion, as shown in Fig. 17. Overall, the TZ81 and TZA810 alloys showed similar corrosion behavior. The corrosion of the TZ81 alloy appeared to be considerably accelerated when the amount of Al contents added to it were as much as 1 – 3wt%. After immersion for 10 minutes, many initiation sites for pitting corrosion were observed in the TZA811 and TZA813 alloys, while only a few pits were found to form in the TZ81 and TZA810 alloys.

In the TZ81 and TZA810 alloys, it can be seen that corrosion was initiated in the typical pitting corrosion mode and then it propagated in the filiform corrosion mode. In the TZA811 and TZA813 alloys, however, both the initiation and propagation of corrosion occurred in the pitting corrosion mode.

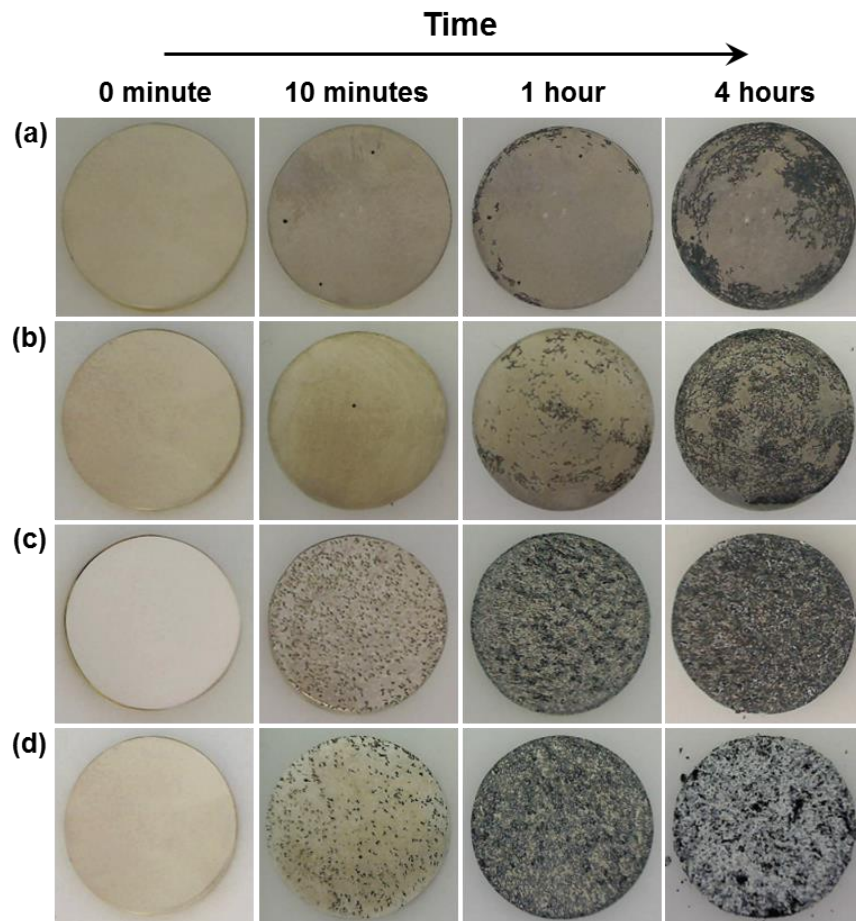


Fig. 17. Optical micrographs showing the macroscopic surfaces of the extruded alloys before and after immersion in 0.6M NaCl solution: (a) TZ81, (b) TZA810, (c) TZA811, and (d) TZA813.

To investigate the causes of severe corrosion on TZA811, TZA813 alloys, the before and after immersion microstructures of each alloy were observed and compared by SEM. SEM micrographs in Fig. 18 disclose that no serious corrosion occurred around either Mg_2Sn or $AlFe$ particles in the TZA810 alloy after immersion for 20 minutes. In the TZA811 and TZA813 alloys, on the other hand, fairly severe corrosion was found to occur at positions where Al_5Fe_2 particles existed, even after the relatively short immersion time of 4 minutes. This clearly indicates that these particles act as preferred pitting corrosion sites during immersion in 0.6 M NaCl solution, which can lead to the acceleration of corrosion kinetics.

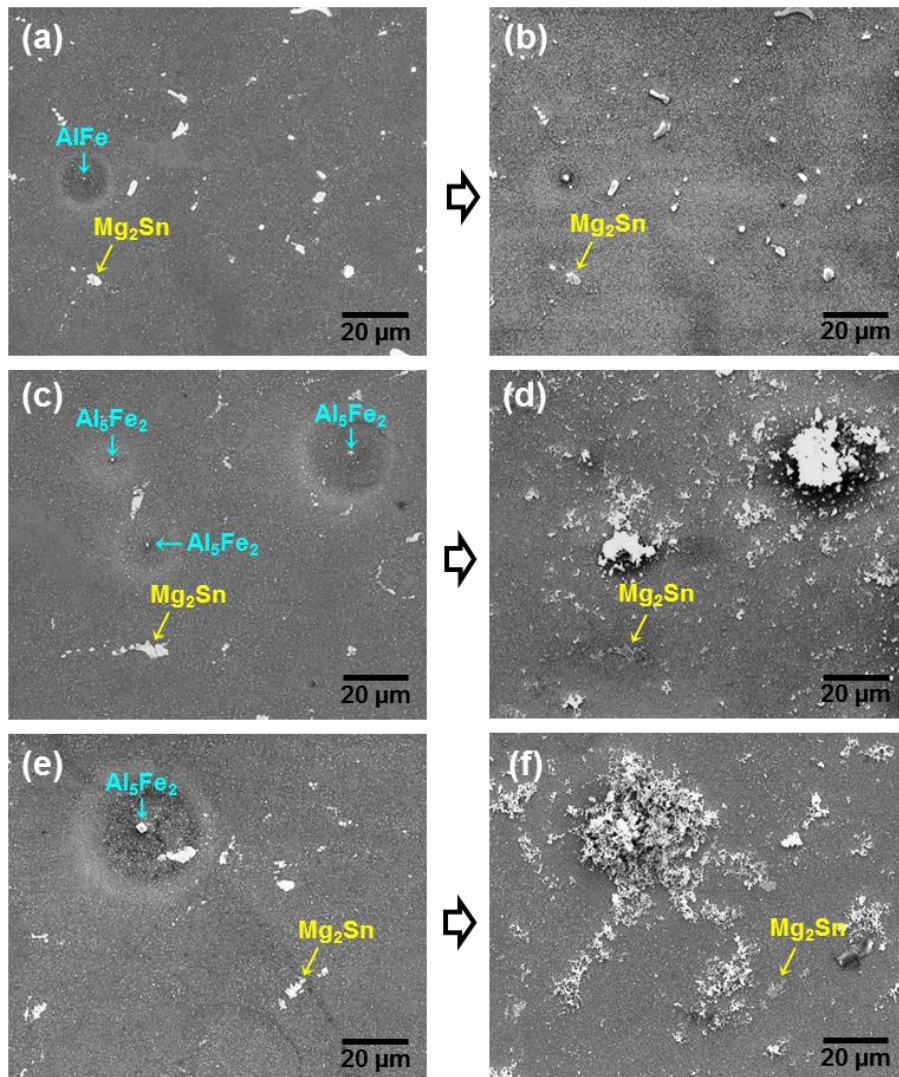


Fig. 18. SEM micrographs showing the surfaces of the extruded alloys before and after immersion in 0.6 M NaCl solution: the TZA810 alloy (a) before and (b) after immersion for 20 minutes, the TZA811 alloy (c) before and (d) after immersion for 4 minutes, and the TZA813 alloy (e) before and (f) after immersion for 4 minutes.

Overall corrosion rates were calculated after immersion for 72 hours, and are shown in Fig. 19; they are 7.8 ± 0.6 , 5.6 ± 0.6 , 247 ± 4.7 , and 322 ± 7.5 mm y⁻¹ for the TZ81, TZA810, TZA811, and TZA813 alloys, respectively. It is interesting to note that the additions of 1 – 3wt% Al to the TZ81 alloy leads to a significant degradation of corrosion resistance whereas the addition of 0.3wt% Al has a somewhat beneficial effect on corrosion resistance. Surprisingly, the rate of corrosion of the TZA811 alloy was about 44 times faster than that of the TZA810 alloy, although the difference in the Al content between the two alloys was merely 0.7wt%. The difference of corrosion properties between TZA810 alloy and TZA811, TZA813 alloys would be investigated by other corrosion tests.

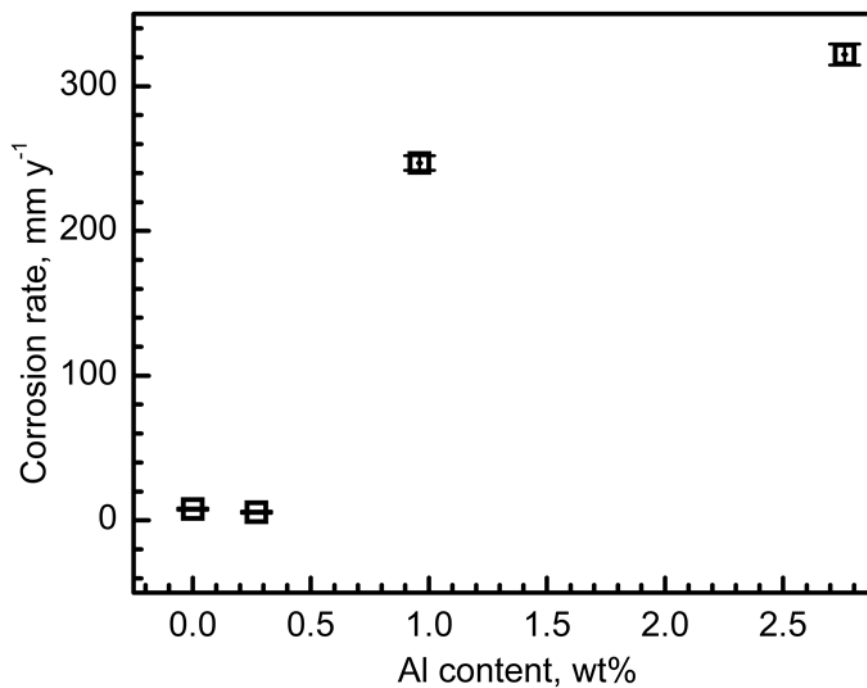


Fig. 19. Corrosion rates of the extruded alloys with different Al contents, which were measured by immersion in 0.6 M NaCl solution for 72 hours.

3.3.3. E_{corr} monitoring

Fig. 20 shows variations in the E_{corr} level, which were monitored during 300 seconds in 0.6 M NaCl solution. The E_{corr} levels appear to increase in a parabolic manner, indicating that spontaneous passivity occurred under the open circuit condition. It also shows that E_{corr} levels tend to increase as the Al content increases. Although the addition of 0.3wt% Al to the TZ81 alloy did not markedly increase the E_{corr} level, the additions of 1 – 3wt% Al resulted in a considerable increase in the E_{corr} level. However, the E_{corr} levels of the TZA811 and TZA813 alloys were found to drop after immersion times of 120 and 80 seconds, respectively. This suggests that the passive films formed on these alloys can be easily broken, which is consistent with the immersion test results given above. As shown in Fig. 17, pitting corrosion readily occurred in the TZA811 and TZA813 alloys even after 10 minutes in 0.6 M NaCl solution, while it was rarely observed in the TZ81 and TZA810 alloys after such a short immersion time.

To account for the rise in the E_{corr} level with Al addition, two possibilities are conceivable; one is the promotion of passivity and the other is the acceleration of the H_2 evolution rate. If the effects of Al addition on the passivity and H_2 evolution rate can be clarified, then the decreased induction time to passivity breakdown following the Al addition could be well explained. Thus, potentiodynamic polarization tests were carried out to more clearly understand the results from the immersion tests and the E_{corr} monitoring. Based on the results in Fig. 20, polarization curves were obtained immediately after immersion, because the breakdown of passive films during immersion was found to occur very rapidly in the TZA811 and TZA813 alloys.

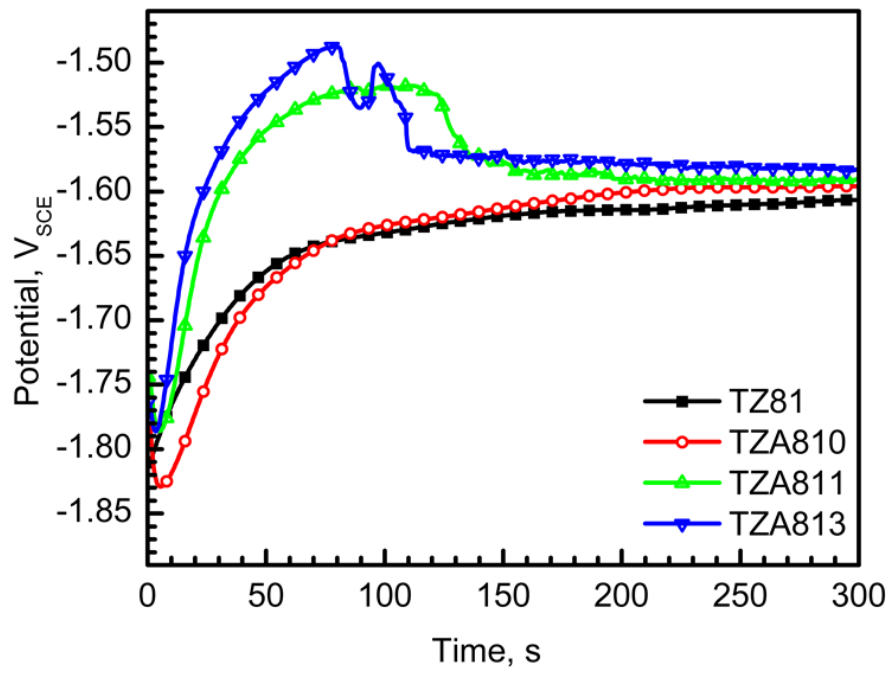


Fig. 20. Corrosion potential transition curves of the extruded alloys.

3.3.4. Potentiodynamic polarization tests in 0.6 M NaCl solution

Fig. 21a shows the polarization curves obtained in 0.6 M NaCl solution. In the TZ81 and TZA810 alloys, passivity appears at their E_{corr} levels, and the difference between their E_{pit} levels is marginal. On the other hand, the polarization curves of the TZA811 and TZA813 alloys demonstrate that pitting corrosion occurs at (or under) their E_{corr} levels. The E_{corr} levels are -1.69, -1.67, -1.56, and -1.54 V_{SCE} for the TZ81, TZA810, TZA811, and TZA813 alloys, respectively, showing good agreement with the E_{corr} monitoring results in Fig. 20.

When considering the passive current density (i_{passive}) levels of the TZ81 and TZA810 alloys, it was noticed that the addition of 0.3wt% Al slightly decreased the i_{passive} level. However, the i_{passive} levels of the TZA811 and TZA813 alloys cannot be compared by using these polarization curves since their pitting corrosion occurs at (or under) their E_{corr} levels, as mentioned above. Due to the formation of passivity, it is not possible to estimate the metal dissolution rate of the alloys using the calculated corrosion current density, which can be evaluated by the Tafel extrapolation method.

If the passive films of the TZ81 and TZA810 alloys are stable, the dissolution rate of these alloys would be equal to i_{passive} at their E_{corr} levels. After passivity breakdown, however, estimating the dissolution rate by using the polarization curves is impossible, which is the case for the TZA811 and TZA813 alloys. Instead, it is possible to compare the H_2 evolution rates of the alloys by measuring the cathodic current density. The cathodic current density levels of the alloys, which were measured at -1.80 V_{SCE} , are given in Fig. 21b. Similar to the immersion test results, the H_2 evolution rates were significantly increased in the TZ81 alloy with the additions of 1 – 3wt% Al, while there was a slight increase in the H_2 evolution rate with the addition of 0.3wt% Al.

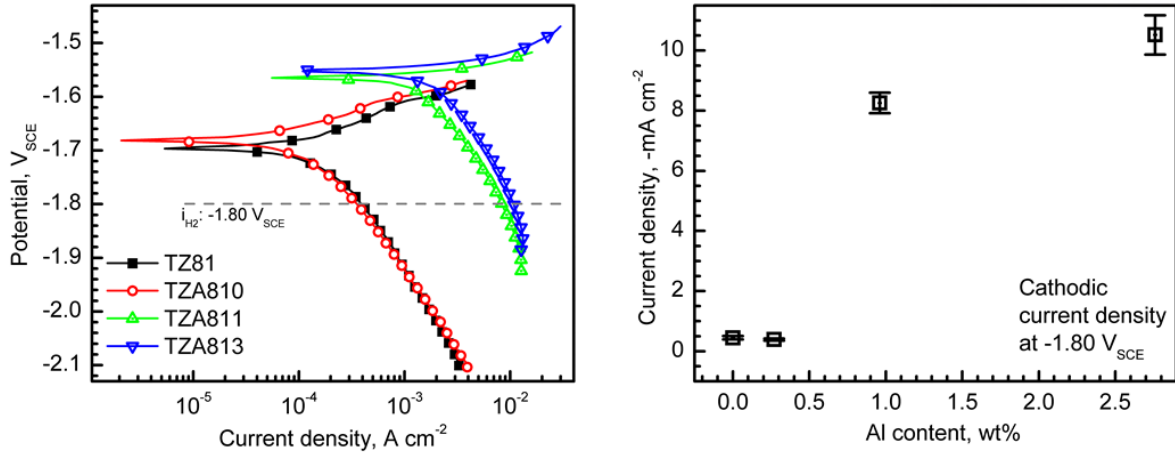


Fig. 21. (a) Polarization curves of the extruded alloys in 0.6 M NaCl solution and (b) cathodic current density values measured from the polarization curves at $-1.80 V_{SCE}$.

3.3.5. Potentiodynamic polarization tests in 0.005 M NaCl solution

Since the 0.6 M NaCl solution was not considered an appropriate subject for the examination of the protectiveness of passive films as mentioned above, polarization tests were performed in a more dilute NaCl solution. Fig. 22a shows E_{corr} transition curves measured in 0.005 M NaCl solution. Similar to the results in Fig. 20, Al addition had a positive effect on the E_{corr} level of the TZ81-based alloys and this effect appeared more pronounced between the TZA810 and TZA811 alloys. In this relatively dilute solution, all the alloys exhibited passivity at their E_{corr} levels, lasting at least 100 seconds.

Polarization curves given in Fig. 22b also reveal that passivity occurred at their E_{corr} levels. Thus, it is possible to compare the $i_{passive}$ levels and E_{pit} levels of the alloys. Although the exact $i_{passive}$ levels cannot be compared because the E_{pit} levels of the TZ81 and TZA810 alloys are lower than the E_{corr} levels of the TZA811 and TZA813 alloys, it can be verified that the $i_{passive}$ levels of the TZA811 and TZA813 alloys are much lower than those of the TZ81 and TZA810 alloys. Fig. 22c shows the variations of the E_{pit} level as a function of Al content; the E_{pit} levels appear to increase as the Al content increases. Considering the variations of $i_{passive}$ and the E_{pit} levels, it can be assumed that solutionized Al in the α -Mg matrix acts as an effective passivator in the corrosion process of the TZ81-based alloys.

In terms of the H₂ evolution rate, the variations of the cathodic current density with Al addition (Fig. 22d), measured at -1.70 V_{SCE}, look similar to those measured in 0.6 M NaCl solution (Fig. 21b). This shows that in 0.005 M NaCl solution, the H₂ evolution rate was also significantly accelerated by the additions of 1 – 3wt% Al, while such an increase in the H₂ evolution rate was not observed in the alloys with less than 0.3wt% Al. When the results which show a decrease in *i*_{passive} and an increase in H₂ evolution rate with the Al addition are considered together, it becomes understandable why the E_{corr} level of the TZ81 alloy was slightly increased by the addition of 0.3wt% Al, and was significantly increased by the additions of 1 – 3 wt% Al.

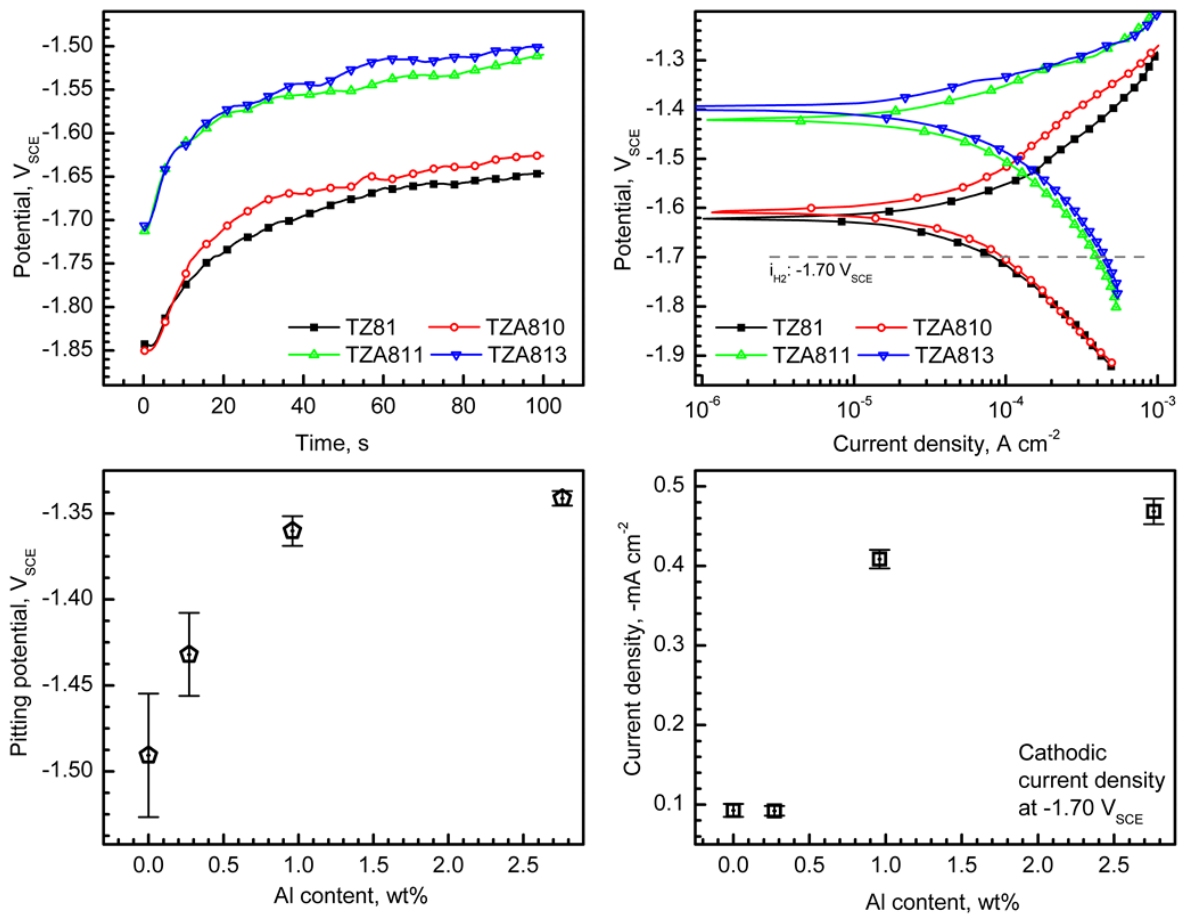


Fig. 22. (a) Corrosion potential transition curves and (b) polarization curves of the extruded alloys in 0.005 M NaCl solution with (c) pitting potential values and (d) cathodic current density values from the polarization curves.

3.4. Discussion

3.4.1. Corrosion-controlling factor

Observations of the corroded samples in 0.6 M NaCl solution indicated that the passive films formed on the TZA811 and TZA813 alloys are not stable, becoming broken after even a short immersion time of 4 minutes. Moreover, the corrosion rates of these alloys with 1 – 3wt% Al were much faster than those of TZ81 and TZA810 alloys with less than 0.3wt% Al. However, the results in Fig. 22(b) and Fig. 22(c), obtained in 0.005 M NaCl solution, obviously show that the alloyed Al contributes to promoting passivity. In that case, the long-term immersion test results in Fig. 19 cannot be explained using the variations of i_{passive} or E_{pit} levels. Instead, changes in the H_2 evolution rate with varying Al contents are believed to better reflect the immersion test results.

As shown in Fig. 21b and Fig. 22d, the addition of 0.3wt% Al slightly decreased the cathodic current density, but additions of 1 – 3wt% Al markedly accelerated the H_2 evolution rate. These conflicting phenomena are thought to be caused by a change in the corrosion controlling mode of the TZ81-based alloys, influenced by the Al content, from passivity control to H_2 evolution control.

When passivity is stable, the anodic branch of the polarization curves can explain the Al effect on the passivity; the alloyed Al promotes the passivity and hence the pitting potential is elevated. At this stage, the corrosion rate of the alloy is controlled by passivity. For TZA811 and TZA813 alloys, however, passivity can only resist for a short period of time, within several hundred seconds, as shown in Fig. 17 and Fig. 20. If passivity begins to break down, the bare metal surface of the TZA811 and TZA813 alloys is directly exposed to the solution and then active dissolution will occur at the corrosion crack tip. If so, the metal dissolution rate at the crack tip of the localized corrosion will be controlled by the H_2 evolution rate because the corrosion rate should be equal to the H_2 evolution rate under open circuit potential. For TZA810 alloy, the effect of passivity needs to be considered more. The passivity level of TZA810 is slightly increased compared to TZ81 alloy, as shown in Fig.20. The slight increase in passivity on TZA810 can be a factor for improving the corrosion rate, because the TZA810 alloy has a relatively long induction time. As passivity is also related to H_2 evolution, it was observed that overall corrosion of TZ81-based alloys is controlled by H_2 evolution.

Therefore, the amount of weight loss is closely related to the H_2 evolution rate as shown in Fig. 21, suggesting that the H_2 evolution rate is a decisive factor affecting the corrosion rate of the TZ81-based alloys in 0.6 M NaCl solution.

3.4.2. Influence of intermetallic particles

The extruded TZ81-based alloys have intermetallic particles in the microstructure. They have coarse and fine Mg_2Sn particles in common, and TZA alloys contain Al-Fe particles as well: AlFe in the TZA810 alloy and Al_5Fe_2 in the TZA811 and TZA813 alloys. Regarding the coarse and fine Mg_2Sn particles, a recent report showed that the coarse ones act as a more active site for the initiation of pitting corrosion than the fine ones [16].

Fig. 23 shows Volta potential maps obtained by SKPFM over selected areas of TZA810 and TZA811 alloys, respectively. It reveals that the intermetallic particles have greater Volta potentials than the α -Mg matrix, which has an average Volta potential of 100 mV. The Volta potentials of AlFe and coarse Mg_2Sn particles in the TZA810 alloy are 700 and 450 mV and those of Al_5Fe_2 and coarse Mg_2Sn particles in the TZA811 alloy are 900 and 400 mV, respectively. This indicates that the AlFe or Al_5Fe_2 particles in the TZA alloys can be more preferable sites for pitting corrosion than the Mg_2Sn particles in a corrosive environment. The difference in the Volta potential between the Al_5Fe_2 and Mg_2Sn particles in the TZA811 alloy is as high as 500 mV whereas that between the AlFe and Mg_2Sn particles in the TZA810 alloy is 250 mV. The difference in the Volta potential between the Al_5Fe_2 and α -Mg matrix in the TZA811 alloy is as high as 800 mV whereas that between the AlFe and α -Mg matrix in the TZA810 alloy is 450 mV, suggesting that the presence of the Al_5Fe_2 particles in the TZA811 and TZA813 alloys has a more deleterious effect on corrosion resistance than that of the AlFe particles in the TZA810 alloy does. As experimentally observed in Fig. 18, the accelerated H_2 evolution rate induced by Al addition can be mainly attributed to the presence of the Al_5Fe_2 particles.

The presence of Al_5Fe_2 particles is considered to influence the stability of passivity as well. Although an improvement in passivity with increasing Al content was demonstrated in Fig. 22, the induction time to passivity breakdown was obviously reduced by increasing the Al content in the TZ81 alloy from 1 to 3wt%. As mentioned, the solutionized Al in the α -Mg matrix can act as an effective passivator in the corrosion process. However, Al content in the α -Mg matrix is not believed to be completely homogeneous, and areas in the vicinity of the Al_5Fe_2 particles are possibly deficient in Al, which is due to the diffusion of Al toward the particles in the process of their formation. This can result in the localized breakdown of passive films around the Al_5Fe_2 particles, leading to drastic pitting corrosion combined with their highly noble property.

Also the volume fraction of Al_5Fe_2 particle could be the main factor of deteriorated corrosion properties on TZA811, TZA813 alloys. As mentioned previously, the amount of Al_5Fe_2 particles in TZA811, TZA813 alloys is about 10 times the amount of AlFe particles in TZA810. Therefore, there

are much more initiation sites which can begin the corrosion in TZA811, TZA813 alloys. Then, the corrosion on TZA811, TZA813 alloys takes place all over the position, and the corrosion properties is more accelerated.

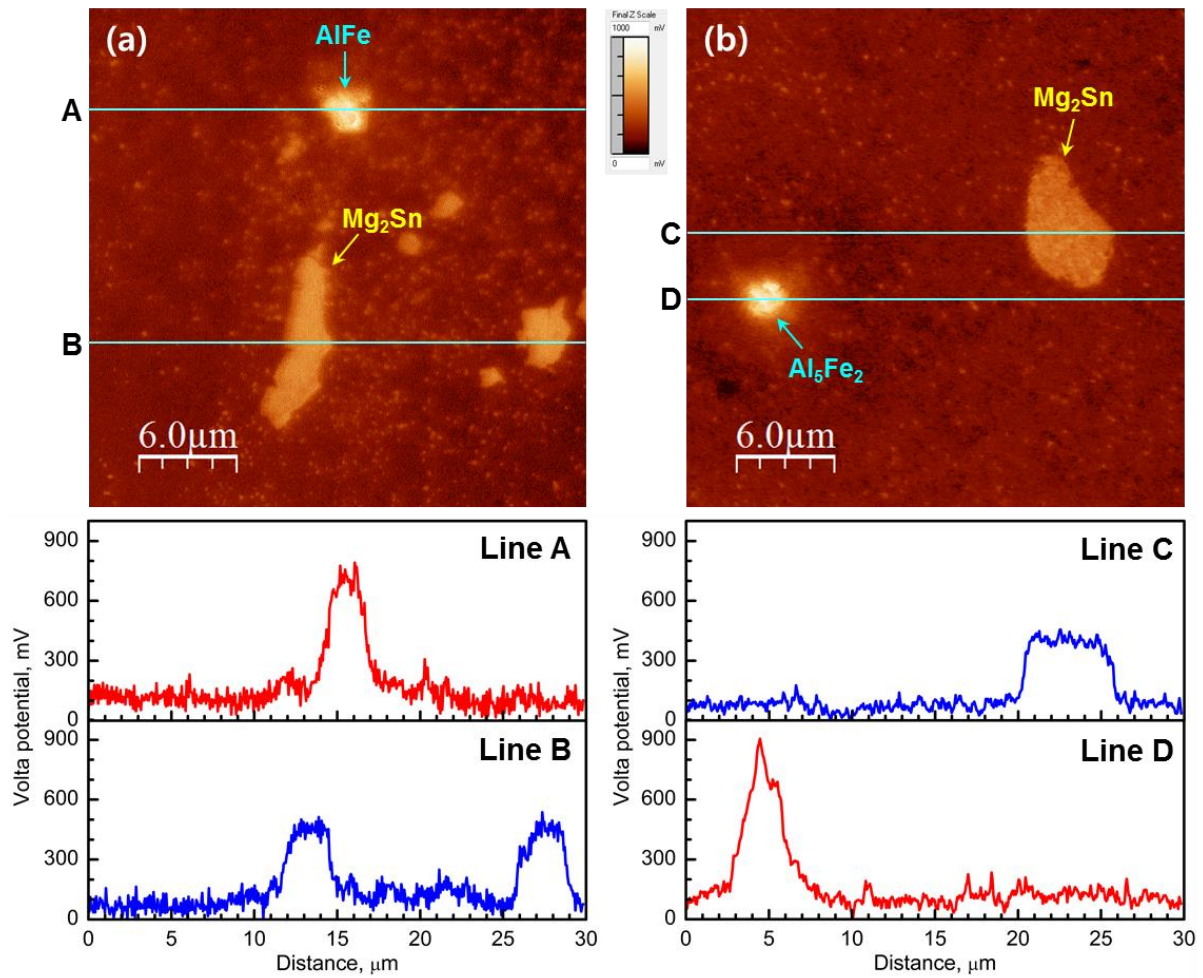


Fig. 23. SKPFM images of the (a) TZA810 and (b) TZA811 alloys and corresponding Volta potential profiles along lines A–D in (a) and (b).

IV. Influence of Mn addition

4.1. Introduction

Previous research on the effect of Al on Mg-8Sn-1Al alloys showed that a specific type of second particle deteriorated the corrosion behavior. Therefore a new alloying element, manganese, is considered as a method for improving the corrosion property of Mg-Sn based alloy.

As I mentioned before, the improving effect of alloyed Mn on corrosion properties is approved in the specific magnesium alloy system. Alloyed Mn element transforms the iron (Fe) or other impurities into harmless intermetallic compounds in AZ series alloys [22]. It is also reported that the amount of Mn then necessary can deteriorate the corrosion properties [24]. Therefore in this study, the small amount manganese is considered as a key factor to improve the corrosion properties of Mg-Sn-Zn-Al alloy.

The microstructure is analyzed with OM, SEM, EPMA, TEM. The corrosion properties are evaluated by immersion tests, potential monitoring, and potentiodynamic tests. The potential of intermetallic is analyzed by SKPFM.

4.2. Experimental

4.2.1. Sample preparation

The analyzed compositions of the Mg-8Sn-1Zn-based alloys used in this study are given in Table 2. Extrusion billets were prepared by induction melting in a graphite crucible under an inert atmosphere with a CO₂ and SF₆ mixture, and subsequent pouring into a steel mould pre-heated to 200 °C. Cast billets were homogenized at 500 °C for 3 hours and then water-quenched. The billets were 80 mm in diameter and 200 mm in length. Indirect extrusion experiments were implemented with an initial billet temperature of 250 °C, a ram speed of 1.3 mm s⁻¹, and an extrusion ratio of 25.

4.2.2. Microstructure characterization

Microstructural examinations were conducted on the midsections of the extruded samples perpendicular to the extrusion direction (ED). Each sample was ground on SiC papers up to 2000 grit under water atmosphere, and then polished using 1 μm diamond paste and 0.04 μm colloidal silica solution under ethanol atmosphere, respectively. The polished samples were chemically etched to reveal grain boundaries using a solution consisting of 10 ml acetic acid, 4.2 g picric acid, 10 ml distilled water, and 70 ml ethanol. Microstructures were observed using a Nikon EPIPHOT 200 optical microscope, a Quanta 200 field-emission scanning electron microscope (SEM) equipped with an energy dispersive spectrometer (EDS), a JEM-2100F Cs-corrected transmission electron microscope (TEM) equipped with EDS, and a JXA-8100 Electron Probe Microanalyzer (EPMA). TEM samples were fabricated using a focused ion beam (FIB) technique.

4.2.3. Electrochemical and immersion tests

The corrosion behavior of the extruded alloys was investigated using immersion tests and potentiodynamic polarization tests at room temperature. The electrochemical tests were conducted at two concentrations of NaCl 0.6 M. The solution for the potentiodynamic polarization tests was deaerated by N_2 purging throughout testing. Prior to the immersion test, the alloy samples were mechanically ground using SiC papers up to 2000 grit. After immersion for 72 hours in 0.6 M NaCl solution the samples were cleaned with 200 g l^{-1} CrO_3 solution and then the weight loss of the samples was measured.

For the electrochemical tests, a conventional three-electrode cell comprising a working electrode (sample), a saturated calomel reference electrode (SCE) and a Pt plate counter electrode was used; the electrochemical tests were conducted using a potentiostat (Reference 600, GAMRY, USA). The samples were ground using SiC papers up to 2000 grit, and an exposed area of 0.13 cm^2 was delineated using electroplating tape. The polarization test was conducted at a scan rate of 1 or 2 mV s^{-1} , and the potential scan started at -0.3 V versus E_{corr} level to each pitting potential (E_{pit}) level of the samples. All electrochemical tests were conducted at least three times to confirm reproducibility.

4.2.4. Scanning Kelvin probe force microscopy

To measure the relative Volta potential differences between second-phase particles and the α -Mg matrix, the potential galvanic interactions between these phases were examined by means of scanning Kelvin probe force microscopy (SKPFM) (XE-70, Park Systems). All of the measurements were performed at room temperature under a controlled relative humidity of $40\pm 5\%$. The Au/Cr-coated conducting tip was modulated by AC modulation of 1.5 V (rms) at frequencies of 17–18 kHz using an external lock-in amplifier (SR-830, Stanford Research Systems). The contact potential difference was obtained by adding a DC feedback voltage to the sample to nullify the electrostatic force component between the tip and the sample, which is proportional to the first harmonic signal of the lock-in amplifier.

4.3. Results

4.3.1. Microstructure

Fig. 24a shows the optical micrograph of extruded TZAM8110 alloy. The microstructure was found to mostly consist of α -Mg grains, which were formed by dynamic recrystallization (DRX) during extrusion. The TZAM8110 alloy shows similar grain sizes to TZA811 alloy in Fig 13c. It indicates that Mn addition has little effect on grain refinement or grain growth. Fig. 24a also shows that second-phase particles are present with the α -Mg grains.

SEM micrographs in Fig. 24b show that two types of Mg_2Sn particles exist in the microstructure; fine precipitates, with a size of several hundreds of nanometers, formed via dynamic precipitation during extrusion; and relatively coarse particles formed during billet casting, which remained even after homogenization prior to extrusion. The SEM micrographs reveal that other kinds of second-particle, denoted as A in Fig 24b is also present in the TZAM8110 alloy. Fig. 24d shows that the second-particle in TZAM8110 alloy mainly consist of Al and Mn, suggesting that the type of second-particle is changed by adding Mn to TZA alloy.

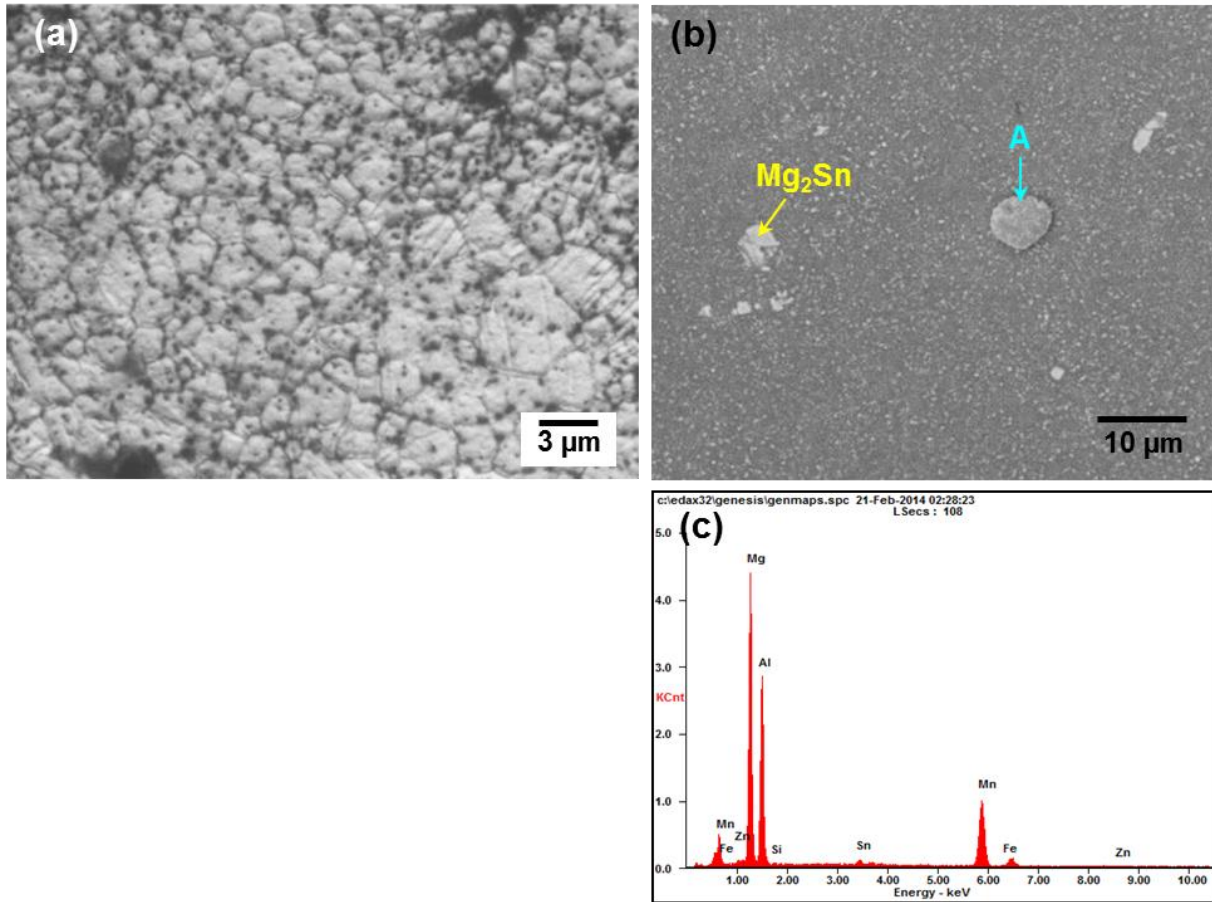


Fig. 24. (a) Optical micrograph, (b) SEM micrograph of the extruded TZAM8110 alloy and (c) EDS spectra of particle labeled A in the TZAM8110 alloy

The change of second particle was also found in the EPMA analysis. Fig 25 shows the EPMA images and corresponding mapping images of alloying elements. In the TZA811 alloy, intermetallic particles that are not Mg_2Sn consist of aluminum and iron, similar to the EDS result in Fig. 16c. In the TZAM8110 alloy, however, EPMA results are not consistent with EDS result in Fig. 24c. Particle A contains not only aluminum and manganese but also iron.

More interestingly, the intermetallic particle in TZAM8110 alloy has core-shell structure. The shell of intermetallic particles in TZAM8110 alloy is composed of aluminum and manganese that are known. The core is composed of aluminum and iron which are similar to the disappeared Al_5Fe_2 particles.

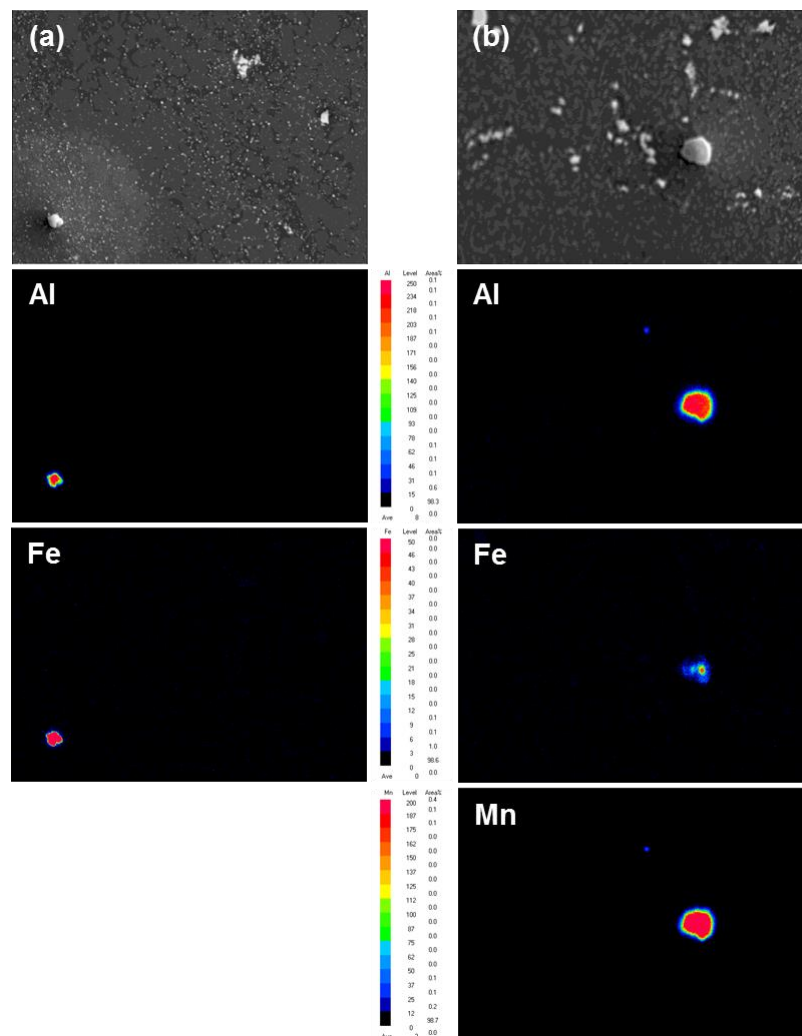


Fig. 25. EPMA images of the (a) TZA811 and (b) TZAM8110 alloys and corresponding Al, Fe, Mn mapping images.

Particle A is more clearly observable with TEM micrographs and EDS analysis in Fig. 26. TEM micrograph and EDS mapping images also show the core – shell structure of intermetallic particles in TZAM8110 alloy. A part of aluminum and manganese is surrounding the part of aluminum and iron. Compositions of core parts are similar to intermetallic particles which accelerate the corrosion rate in TZA811 alloy.

Therefore, the specific types of each part in A particle are confirmed by the electron diffraction patterns, shown in Fig. 26e and Fig. 26f. The particle of '1' region particle in TZAM alloy is identified as Al_3Mn_5 , which has a hexagonal crystal structure with a lattice parameter of $a=1.273\text{nm}$ and $c=1.588\text{nm}$. And the particle of '2' region is identified as $AlFe$, which has a simple cubic structure with a lattice parameter of $a=0.290\text{ nm}$. However it would be rather premature to decide that all intermetallic particles in TZAM8110 alloy have core – shell structure like in Fig 26.

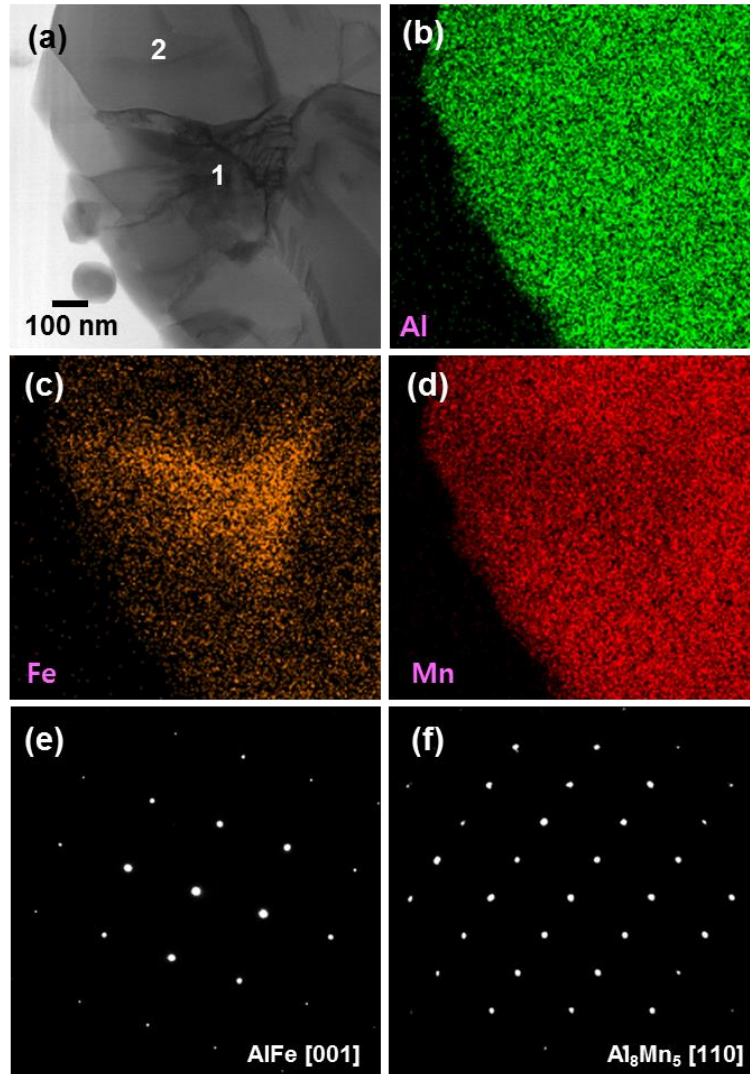


Fig. 26. (a) TEM micrographs of Particle A, corresponding (b) Al, (c) Fe, (d) Mn mapping images, and electron diffraction patterns of (e) '1' region, (f) '2' region.

4.3.2. Immersion test

During immersion in the 0.6 M NaCl solution, extruded TZAM8110 alloy exhibited spontaneous passivity under the open circuit condition, and corrosion was found to begin at points where the passivity broke, resulting in the occurrence of pitting corrosion, as shown in Fig. 27.

Overall, the TZAM8110 alloy shows really different corrosion behavior compared with TZA811 alloy in Fig 17. The corrosion of the TZA811 alloy appeared to be considerably diminished when the 0.1wt% manganese through the addition of 0.1wt% manganese. After immersion for 10 minutes, many initiation sites for pitting corrosion were observed in the TZA811 and TZAM8110 alloys, but the degree and size of pitting corrosion is decrease in TZAM8110 alloy. After immersion for 1 hour, the pitting corrosion is marginally propagated in TZAM8110 alloy, while some pits in TZA811 alloy is extremely accelerated.

In the TZAM8110 alloy, it can be seen that corrosion is initiated in the typical pitting corrosion and then it propagates in the filiform corrosion mode. In the TZA811 alloy, however, both initiation and propagation of corrosion occurred in the pitting corrosion mode.

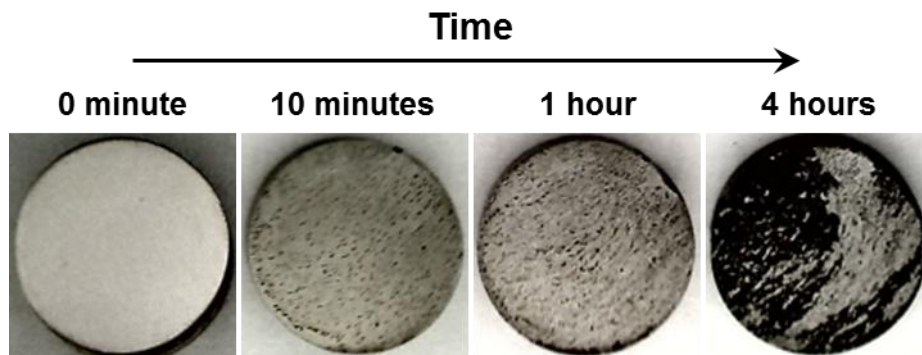


Fig. 27. Optical micrographs showing the macroscopic surfaces of the TZAM8110 extruded alloy before and after immersion in 0.6 M NaCl solution.

SEM micrographs in Fig. 28 disclose that fairly severe corrosion occurred around Al_5Fe_2 particles in the TZA811 alloy after immersion for 4min. In the TZAM8110 alloy, on the other hand, no serious corrosion was found around either Mg_2Sn or Al_8Mn_5 particles, even after the relatively long immersion time of 20 minutes.

These micrographs clearly indicate that Al_8Mn_5 particles in TZAM8110 alloy do not act as strong cathodic sites like Al_5Fe_2 particles in 0.6 M NaCl solution.

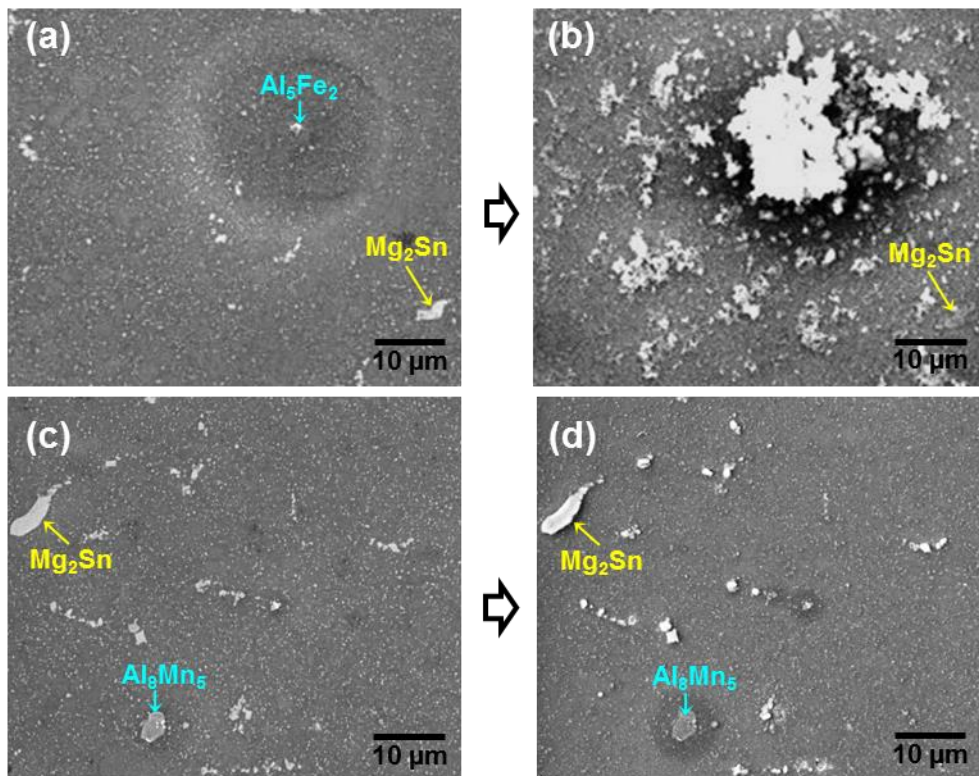


Fig. 28. SEM micrographs showing the surfaces of the extruded alloys before and after immersion in 0.6 M NaCl solution: the TZA811 alloy (a) before and (b) after immersion for 4 minutes, and the TZAM8110 alloy (c) before and (d) after immersion for 20 minutes.

Overall corrosion rates were calculated from hydrogen evolution tests and immersion tests, and are shown in Fig 29. The hydrogen evolution rate is calculated by hydrogen volume per unit area per unit time. They are 87.85 ± 0.84 , and 3.63 ± 0.46 ml cm⁻² h⁻¹ for the TZA811, and TZAM8110 alloys, respectively. Weight loss rate is calculated by the amount of weight loss per unit area for 72 hours. They are 345.82 ± 62.21 , and 9.00 ± 3.42 mg cm⁻² for the TZA811, and TZAM8110 alloys, respectively.

It is interesting to note that the additions 0.1wt% manganese to the TZA811 alloy leads to a significant improvement of corrosion resistance. Only 0.1wt% manganese, a relatively small amount of manganese, surprisingly caused a much slower corrosion rate than that of TZA811 alloy.

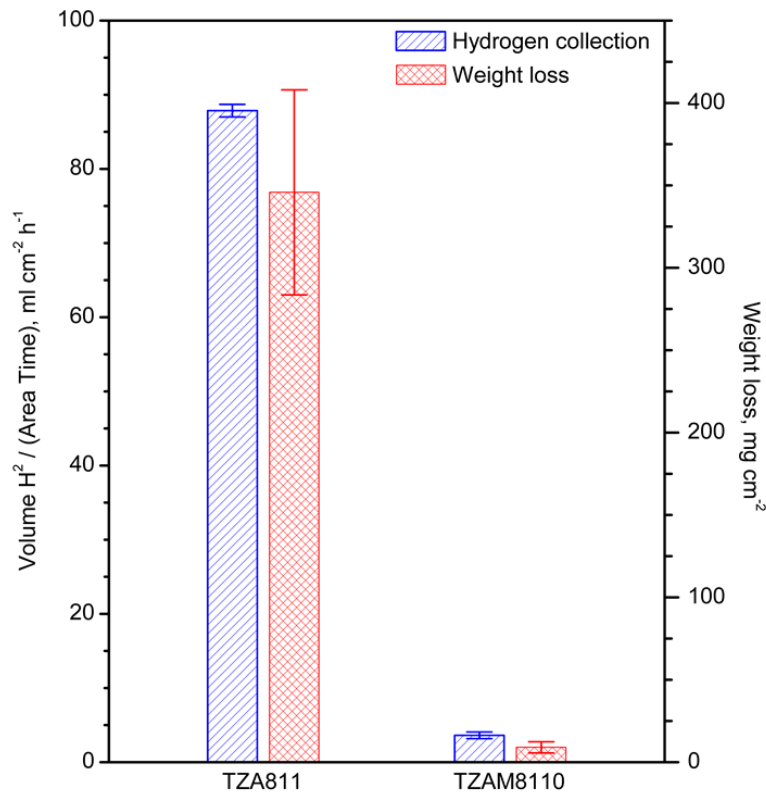


Fig. 29. Corrosion rates of the extruded TZA811 and TZAM8110 alloys which were measured by hydrogen evolution test and immersion test in 0.6 M NaCl solution.

4.3.3. Potentiodynamic polarization tests in 0.6 M NaCl solution

Fig. 30 shows the polarization curves obtained in 0.6 M NaCl solution. The polarization curve of the TZA811 alloy demonstrate that pitting corrosion occurs at (or under) their E_{corr} levels, while TZAM8110 alloy shows the passivity at their E_{corr} levels. Therefore, the comparison of passive current density, i_{passive} , levels of TZA811 and TZAM8110 alloys is not available by polarization curves since pitting corrosion of TZA811 alloy occurs at (or under) their E_{corr} levels.

Instead, it is possible to compare the H_2 evolution rates of the alloys by measuring the cathodic current density. The cathodic current density levels of the alloys can be compared at a specific potential such as $1.80V_{\text{SCE}}$. Similar to the immersion test results, the H_2 evolution rates were significantly decreased in the TZA811 alloy with the addition of 0.1wt% manganese.

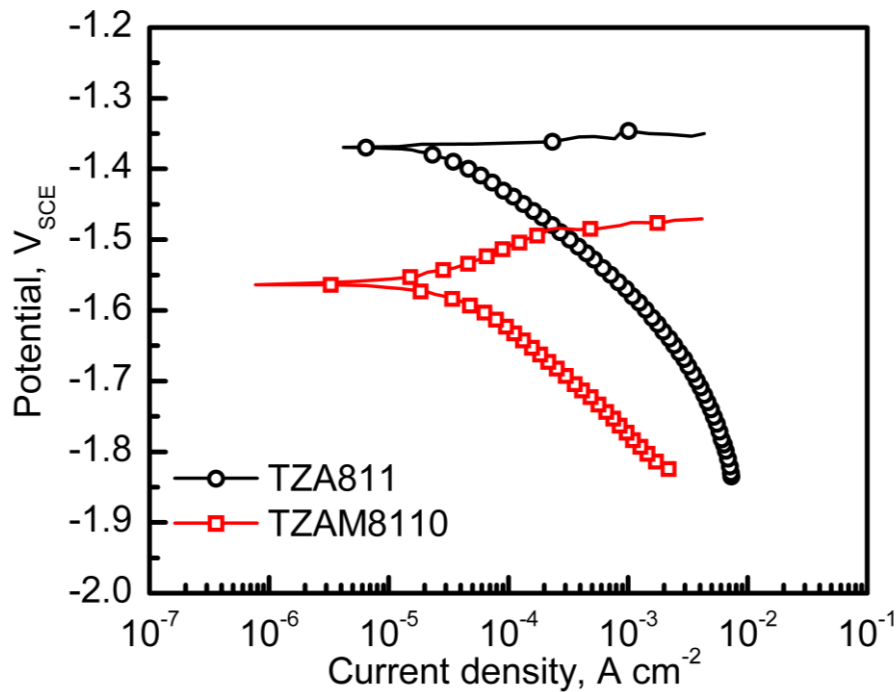


Fig. 30. Polarization curves of the extruded TZA811 and TZAM8110 alloys in 0.6 M NaCl solution.

4.4. Discussion

4.4.1. Influence of intermetallic particles

Fig. 31 shows Volta potential maps obtained by SKPFM over selected areas of TZAM8110 alloy. It reveals that the intermetallic particles have greater Volta potentials than the α -Mg matrix, which has an average Volta potential of 100 mV. The Volta potentials of Al_8Mn_5 and coarse Mg_2Sn particles in the TZAM8110 alloy are 550 and 300 mV, respectively. This indicates that the Al_8Mn_5 particles can be more preferable sites for pitting corrosion than the Mg_2Sn particles in a corrosive environment.

The difference in the Volta potential between the Al_8Mn_5 and Mg_2Sn particles in the TZAM8110 alloy is as high as 250 mV whereas that between the Al_5Fe_2 and Mg_2Sn particles in the TZA811 alloy is 500 mV. The difference in the Volta potential between the Al_8Mn_5 and α -Mg matrix in the TZAM8110 alloy is as high as 450 mV, whereas that between the Al_5Fe_2 and Mg_2Sn particles in the TZA811 alloy is 800 mV, suggesting that the presence of the Al_8Mn_5 particles in the TZAM8110 alloy has a more improving effect on corrosion resistance than that by the Al_5Fe_2 particles in the TZA811 alloy. Therefore, Al_8Mn_5 particles which form by adding manganese make a weaker galvanic couple than Al_5Fe_2 particles.

As mentioned above, it could not be assured that all intermetallic particles in TZAM8110 alloy have core – shell structure, because the observation of all intermetallic particles are not achieved. However, it is certain that the addition of manganese causes the disappearance of Fe-containing particles and the formation of Al_8Mn_5 particles which do not act strong cathodic sites than Al_5Fe_2 particles.

Thus, as one piece of reliable proof, Al_8Mn_5 particles could be surrounding the Fe-containing particles which are strong cathodic sites by making core – shell structure. The Al_8Mn_5 particles also effectively prevent the exposure of the Fe-containing particles, which accelerates the corrosion rates.

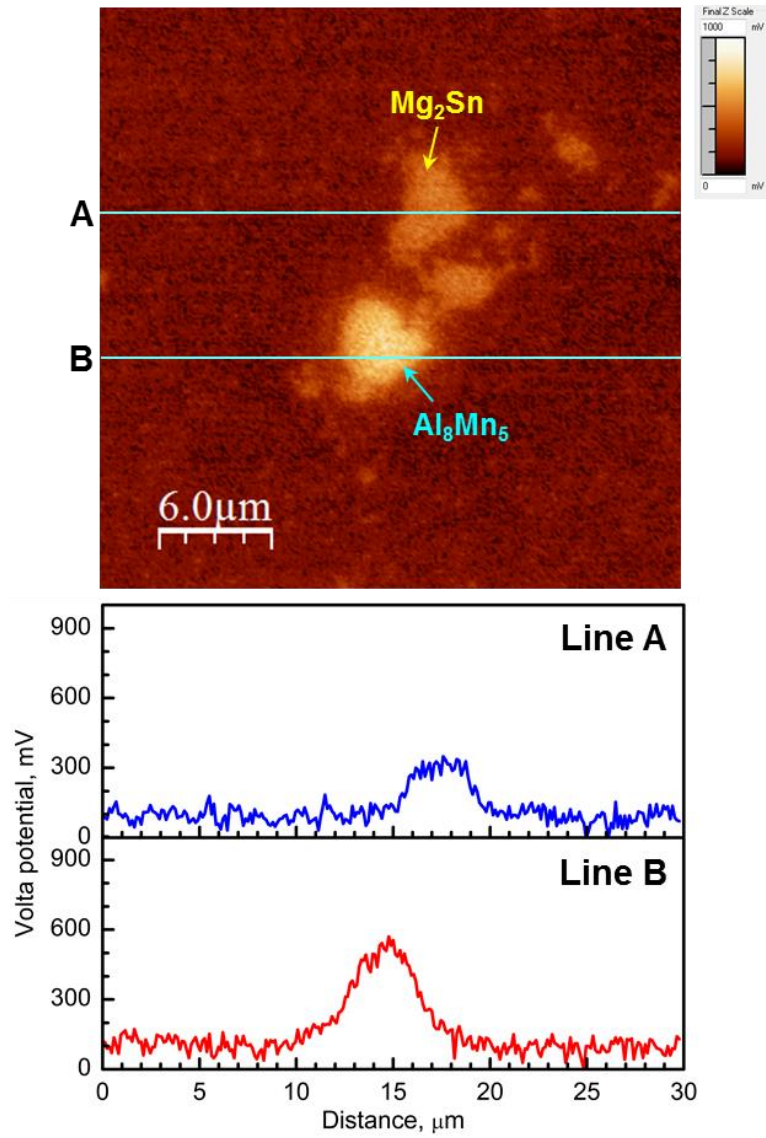


Fig. 31. SKPFM images of the TZAM8110 alloy and corresponding Volta potential profiles along lines A–B.

V. Conclusions

The effects of aluminum added to the microstructure and corrosion properties of extruded TZ81-based alloys were investigated. The microstructures of the extruded alloys mainly consisted of α -Mg grains and Mg_2Sn particles in common. The additions of 0.3 – 3wt% Al to the TZ81 alloy resulted in the formation of Al-Fe-based intermetallic particles as well as grain refinement. Although the addition of 0.3wt% Al resulted in a somewhat improved corrosion resistance, the TZ81 alloy with 1 – 3wt% Al showed over 30 times faster corrosion rates than the TZ81 alloy, in a 0.6 M NaCl solution. The increased corrosion rate with added Al is attributed to the presence of Al_5Fe_2 particles, which act as strong cathodic sites for H_2 evolution during corrosion.

The effects of added manganese on the microstructure and corrosion properties of extruded TZA811-based alloys were also investigated. The microstructure of the extruded alloys mainly consisted of α -Mg grains and Mg_2Sn particles in common. The addition of Mn to the TZA811 alloy resulted in the formation of Al_8Mn_5 particles. The addition of 0.1wt% manganese resulted in the improvement in corrosion resistance of over 40 times in 0.6 M NaCl solution, because intermetallic particles in TZAM8110 alloy have core-shell structure. It could not be confirmed that all intermetallic particles in TZAM8110 alloy have core – shell structure, but it is certain that the addition of manganese causes the disappearance of Fe-containing particles and formation of Al_8Mn_5 particles which do not act as strong cathodic sites than Al_5Fe_2 particles.

A reliable evidence pointing to the improvement of corrosion properties, Al_8Mn_5 particles could be surrounding the Fe-containing particles which are strong cathodic sites by making core – shell structure. The shell of intermetallic particles in TZAM8110 alloy is composed of aluminum and manganese what we have been known. And the core is composed of aluminum and iron which are similar to the disappeared Al_5Fe_2 particles. The Al_8Mn_5 particles can effectively prevent the exposure of the Fe-containing particles and make a less strong galvanic couple than Al_5Fe_2 particles which accelerate the corrosion rate. As a result, the addition of aluminum and manganese can cause significantly positive effects on corrosion behavior in TZ alloys.

VI. References

- [1] Y. Kojima, Platform science and technology for advanced magnesium alloys. *Mater. Sci. Forum*, 350-351 (2000) 3-18.
- [2] R.C. Zeng, J. Zhang, W.J. Huang, W. Dietzel, K.U. Kainer, C. Blawert, K.E. Wei, Review of studies on corrosion of magnesium alloys, *T. Nonferr. Soc.* 16 (2006) s763-s771
- [3] D.H. Kang, S.S. Park, N.J. Kim, Development of creep resistant die cast Mg–Sn–Al–Si alloy, *Mater. Sci. Eng. A* 413–414 (2005) 555–560.
- [4] D.H. Kang, S.S. Park, Y.S. Oh, N.J. Kim, Effect of nano-particles on the creep resistance of Mg–Sn based alloys, *Mater. Sci. Eng. A* 449–451 (2007) 318–321.
- [5] S. Wei, Y. Chen, Y. Tang, H. Liu, S. Xiao, G. Niu, X. Zhang, Y. Zhao, Compressive creep behavior of as-cast and aging-treated Mg–5wt% Sn alloys, *Mater. Sci. Eng. A* 492 (2008) 20–23.
- [6] B.H. Kim, S.W. Lee, Y.H. Park, I.M. Park, The microstructure, tensile properties, and creep behavior of AZ91, AS52 and TAS652 alloy, *J. Alloy. Compd.* 493 (2010) 502–506.
- [7] M.A. Gibson, X. Fang, C.J. Bettles, C.R. Hutchinson, The effect of precipitate state on the creep resistance of Mg–Sn alloys, *Scripta Mater.* 63 (2010) 899–902.
- [8] W.L. Cheng, S.S. Park, B.S. You, B.H. Koo, Microstructure and mechanical properties of binary Mg–Sn alloys subjected to indirect extrusion, *Mater. Sci. Eng. A* 527 (2010) 4650–4653.
- [9] D. Chen, Y. Ren, Y. Guo, W. Pei, H. Zhao, G. Qin, Microstructures and tensile properties of as-extruded Mg–Sn binary alloys, *T. Nonferr. Soc.* 20 (2010) 1321–1325.
- [10] T.T. Sasaki, K. Oh-ishi, T. Ohkubo, K. Hono, Enhanced age hardening response by the addition of Zn in Mg–Sn alloys, *Scripta Mater.* 55 (2006) 251-254
- [11] T.T. Sasaki, J.D. Ju, K. Hono, K.S. Shin, Heat-treatable Mg–Sn–Zn wrought alloy, *Scripta Mater.* 61 (2009) 80–83.
- [12] W.N. Tang, S.S. Park, B.S. you, Effect of the Zn content on the microstructure and mechanical properties of indirect-extruded Mg–5Sn–xZn alloys, *Mater. Design* 32 (2011) 3537–3543.

- [13] T.T. Sasaki, K. Yamamoto, T. Honma, S. Kamado, K. Hono, A high-strength Mg–Sn–Zn–Al alloy extruded at low temperature, *Scripta Mater.* 59 (2008) 1111–1114.
- [14] S.S. Park, W.N. Tang, B.S. You, Microstructure and mechanical properties of an indirect-extruded Mg–8Sn–1Al–1Zn alloy, *Mater. Lett.* 64 (2010) 31–34.
- [15] W.L. Cheng, H.S. Kim, B.S. You, B.H. Koo, S.S. Park, Strength and ductility of novel Mg–8Sn–1Al–1Zn alloys extruded at different speeds, *Mater. Lett.* 65 (2011) 1525–1527.
- [16] S.S. Park, B.S. You, Low-temperature superplasticity of extruded Mg–Sn–Al–Zn alloy, *Scripta Mater.* 65 (2011) 202–205.
- [17] H.-Y. Ha, J.-Y. Kang, S.G. Kim, B. Kim, S.S. Park, C.D. Yim, B.S. You, Influences of metallurgical factors on the corrosion behaviour of extruded binary Mg–Sn alloys, *Corros. Sci.* 82 (2014) 369–379.
- [18] H.-Y. Ha, J.-Y. Kang, C.D. Yim, J. Yang, B.S. You, Role of hydrogen evolution rate in determining the corrosion rate of extruded Mg–5Sn–(1–4 wt%)Zn alloys, *Corros. Sci.* 89 (2014) 275–285.
- [19] Z.B. Sajuri, Y. Miyashita, Y. Hosokai, Y. Mutoh, Effects of Mn content and texture on fatigue properties of as-cast and extruded AZ61 magnesium alloys, *Int. J. Mech. Sci.* 48 (2006) 198–209
- [20] M. Lugo, J.B. Jordon, K.N. Solanki, L.G. Hector Jr, J.D. Bernard, A.A. Luo, M.F. Horstemeyer, Role of different material processing methods on the fatigue behavior of an AZ31 magnesium alloy, *Int. J. Fatigue* 52 (2013) 131–143
- [21] M.A. Azeem, A. Tewari, U. Ramamurty, Effect of recrystallization and grain growth on the mechanical properties of an extruded AZ21 Mg alloy, *Mater. Sci. Eng. A* 527 (2010) 898–903
- [22] G. L. Song, A. Atrens, Corrosion mechanisms of magnesium alloys, *Adv. Eng. Mater.* 1 (1999) 11–33.
- [23] X. Gu, Y. Zheng, Y. Cheng, S. Zhong, T. Xi, In vitro corrosion and biocompatibility of binary magnesium alloys, *Biomaterials* 30 (2009) 484–498.
- [24] N. D. Nam, M. Mathesh, M. Forsyth, D. S. Jo, Effect of manganese additions on the corrosion behavior of an extruded Mg–5Al based alloy, *J. Alloys Compd.* 542 (2012) 199–206.
- [25] E. Ghali, *Uhlig's Corrosion Handbook* (Ed: R. W. Revie), Wiley (2000) 793.

- [26] O. Lunder, K. Nisancioglu, R.S. Hanses, SAE Technical Paper No. 930755 (1993).
- [27] G. Song, A. Atrens, M. Dargusch, Influence of microstructure on the corrosion of diecast AZ91D, *Corros. Sci.* 41 (1999) 249-273.
- [28] R.C. Zeng, W.Q. Zhou, E.H. Han, W. Ke, Effect of pH value on corrosion of as-extruded AM60 magnesium alloy, *Acta Metall. Sinica* 44(3) (2005) 307-311.
- [29] R.T. Ruggeri, T.R. Beck, An analysis of mass transfer in filiform corrosion, *Corrosion* 39 (1983) 452–465.
- [30] P. Schmutz, V. Guillaumin, R.S. Lillard, J.A. Lillard, G.S. Frankel, Influence of dichromate ions on corrosion processes on pure magnesium, *J. Electrochem. Soc.* 150 (2003) B99–B110.
- [31] O. Lunder, J.E. Lein, S.M. Hesjevik, Kr. Aune, K. Nisancioglu, Corrosion morphologies on magnesium alloy AZ91, *Mater. Corros.* 45 (1994) 331-340.
- [32] T. Valente, Grain boundary effects on the behavior of WE43 magnesium castings in simulated marine environment, *J. Mater. Sci. Lett* 20 (2001) 67-69.
- [33] E. Ghali, W. Dietzel, K.U. Kainer, General and localized corrosion of magnesium alloys: a critical review, *J. Mater. Eng. Perf.* 13(1) (2004) 7-23.
- [34] Y. Ding, C. Wen, P. Hodgson, Y. Li, Effects of alloying elements on the corrosion behavior and biocompatibility of biodegradable magnesium alloys: a review, *J. Mater. Chem. B* 2 (2014) 1912-1933.
- [35] A.D. Südholz, N. Birbills, C.J. Bettles, M.A. Gibson, Corrosion behavior of Mg-alloy AZ91E with atypical alloying additions, *J. Alloy. Compd.* 471 (2009) 109–115
- [36] W.E. Mercer, J.E. Hillis, SAE Technical Paper No. 920073 (1992).
- [37] ASTM standards G1-31, Standard practice for preparing cleaning and evaluating corrosion test specimens.
- [38] R. Baboian, *Electrochemical Techniques for corrosion Engineering*, National Association of Corrosion Engineers (1986).
- [39] S.L. Gebremedhin, J.R. Shroeder, *Laboratory Corrosion Test and Standards*, ASTM, Philadelphia, PA 19103

- [40] H. Huo, Y. Li, F. Wang, Corrosion of AZ91D magnesium alloy with a chemical conversion coating and electroless nickel layer, *Corros. Sci.* 46 (2004) 1467-1477
- [41] G.L. Song, A. Atrens, Understanding magnesium corrosion – A framework for improved alloy performance, *Adv. Eng. Mater.* 5 (2003) 837-858.